Low Complexity Super-Resolution OTFS-Assisted ISAC Framework for THz Communication

Hanem Hegazy, *Graduate Student Member, IEEE*, Abdelfatah Abdelbar, *Graduate Student Member, IEEE*, Ibrahim Al-Nahhal, *Senior Member, IEEE*, and Octavia A. Dobre, *Fellow, IEEE*

***Abstract*—Integrated sensing and communication (ISAC) in terahertz (THz) is a promising technology that supports simultaneous terabit-per-second data transmission and millimeter-level precision sensing. However, THz ISAC systems face significant challenges, including severe Doppler shifts and reduced power amplifier efficiency due to a high peak-to-average power ratio (PAPR). This paper presents a super-resolution orthogonal time frequency space-assisted ISAC (SR-OTFS-ISAC) framework aimed at enhancing robustness against Doppler effects in multipath THz channels. The framework effectively addresses both integer and fractional delay and Doppler. The proposed framework incorporates a low-complexity super-resolution sensing technique that begins with denoising the received signals using a super-resolution deep neural network (SR-DNN) for precise path detection. This is followed by a coarse estimation of the dominant paths using the max-path phase. This estimate is then refined using an alternative optimization (AO) method to improve the accuracy of the delay-Doppler (DD) parameters. This approach, called the super-resolution max-path alternative optimization (SR-M-PAO) method, provides better channel estimates. These enhanced estimates support multi-target sensing, transmitter localization, and data detection using a conjugate gradient algorithm. The proposed SR-OTFS design enables channel estimation, parameters sensing and data detection within a single OTFS frame. Additionally, computational complexity is derived in terms of the required real addition and multiplication operations, offering clear insights into the proposed algorithm's efficiency. Simulation results demonstrate that the SR-OTFS-ISAC framework delivers range estimation accuracy at the millimeter scale and velocity estimation precision at the centimeter-per-second level, all while ensuring lower computational complexity. Furthermore, it achieves an approximate 1.7 dB reduction in PAPR compared to the literature while maintaining a robust performance bit error rate, even under fractional DD effects.**

***Index Terms*—Orthogonal time frequency space (OTFS), terahertz integrated sensing and communication (THz ISAC), embedded pilot, channel estimation, alternative optimization (AO), super-resolution deep neural network (SR-DNN).**

This work was supported in part by the Natural Sciences and Engineering Research Council of Canada (NSERC) Discovery Grant RGPIN-2019-04123 and in part by the Canada Research Chair program under Grant CRC-2022-00187. An earlier version of this paper was presented in part at the 2025 IEEE Interna-tional Conference on Communications (ICC). The review of this article was coordinated by Prof. Qingqing Wu. *(Corresponding author: Octavia A. Dobre.)*

The authors are with the Faculty of Engineering and Applied Science, Memorial University, St. Johns, NL A1C 5S7, Canada (e-mail: hihegazy@mun.ca; abdelfatahm@mun.ca; ioalnahhal@mun.ca; odobre@mun.ca).

I. Introduction

THE rapid expansion of wireless communication networks coupled with increasing demand for high data rates, low latency, and massive connectivity, has led to considerable attention being focused on the terahertz (THz) frequency range. With its extensive bandwidth and unique propagation behavior spanning from 0.1 to 10 THz, this spectrum holds immense potential to enable cutting-edge wireless technologies, such as 6G networks. However, THz also presents unique challenges. THz waves face several propagation challenges, including high free-space path loss, susceptibility to molecular absorption, and limited diffraction. These factors have a significant impact on achieving reliable communication over long distances and require careful system design to overcome these limitations.

Integrated Sensing and Communication (ISAC) enhances THz communication by combining high-resolution sensing and ultra-fast data transmission in a single system [1]. It enables real-time environmental awareness, improving beamforming, blockage prediction, and mobility management—crucial for high-mobility applications like autonomous systems, healthcare, and vehicular networks [2].

THz ISAC faces major challenges in high-mobility environments, particularly with maintaining stable links due to complex interference between sensing and communication. Precise beam alignment and efficient spectrum sharing are crucial. High Doppler effects in such scenarios cause rapid channel variations [3] and inter-carrier interference (ICI), especially in time-frequency domain (TF) modulation schemes like orthogonal frequency division multiplexing (OFDM) and discrete Fourier transform spread OFDM (DFT-s-OFDM), leading to degraded performance, higher BER, and reduced throughput. Traditional OFDM radar processing may also fail to accurately detect fast-moving targets, impacting sensing reliability.

Moreover, as 6G networks aim to make substantial improvements in the energy efficiency, achieving this within THz ISAC systems is a challenge. At higher operational frequencies, power amplifiers (PAs) experience a notable reduction in their maximum output power, even with advancements in integrated circuit technology [4].

A. Related Work

The idea of ISAC has attracted substantial research attention, primarily driven by the need for highly efficient, multifunctional wireless systems. Recent advances in waveform design have propelled the shift toward a truly integrated framework. In [5], the authors introduced the concept of joint waveform design for the ISAC system, where a single waveform performs both communication and sensing functions. This unified design enhanced the spectral efficiency and improved the energy efficiency by reducing the need for separate signal processing blocks.

Another key development in ISAC research is the integration of ISAC with machine learning (ML) techniques. As explored in [6], ML algorithms, particularly deep learning, have been employed to optimize resource allocation, waveform design, and signal processing in ISAC systems. ML-based methods have shown promise in overcoming the complex trade-offs between sensing and communication by dynamically adapting system parameters based on real-time environmental conditions.

In recent literature, various approaches have been proposed for ISAC implementation. For example, [7] presented an OFDM-based ISAC framework that employs the two-dimensional fast Fourier transform (FFT) and the multiple signal classification method. Additionally, [8], demonstrated the feasibility of employing correlation-based radar processing techniques to extract radar sensing parameters from OFDM baseband signals. However, the OFDM-based ISAC systems face challenges such as PAPR and ICI.

Recently, the orthogonal time frequency space (OTFS) modulation has emerged as a promising approach to address these challenges [9]. The OTFS modulation provides significant advantages over OFDM in multipath delay Doppler (DD) channels by representing the time-varying nature of these channels in the DD domain. By distributing information symbols on a two-dimensional orthogonal basis, OTFS is designed to handle the dynamics of multipath channels that vary in time more effectively than traditional methods [10]. Meanwhile, the research in [11] demonstrates the successful application of OTFS modulation within the framework of ISAC. To enable OTFS detection, an accurate estimation of the DD channel is crucial, as discussed in [10], [12], [13], [14], [15], [16]. Consequently, pilot-aided channel estimation techniques have been explored in studies such as [12], [17], [18], [19], [20], [21], [22].

In [17], pilot transmission was carried out using a dedicated OTFS frame, with the estimated channel information applied for data detection in the subsequent frame. However, this approach may become ineffective if the channel estimation is outdated in the next frame. In contrast, channel estimation in the TF domain was performed in [19], although this leads to a higher implementation complexity compared to [17], [18], where estimation was performed in the DD domain. In [18], channel estimation was specifically considered for OTFS using an ideal pulse-shaped waveform over channels with integer Doppler shifts.

In [20], an OTFS frame structure based on embedded pilot (EP) was presented. The arrangement of guard symbols is designed to mitigate interference from data symbols, ensuring the integrity of the pilot symbol. In this instance, the addition of guard symbols lowers the spectral efficiency and causes a non-negligible DD resource overhead. In [12], [21], [22], superimposed pilot design schemes were devised; nevertheless, [12] continued to estimate the delay and Doppler parameters using the EP frame, while [21] did not take fractional delay and Doppler into account.

The iterative method in [22] improves channel estimation and data detection using pilots, but it mainly targets active sensing and faces several issues: high complexity due to iterative refinement and exhaustive search, especially for large OTFS frames, and performance degradation at higher modulation orders due to increased interference between data and pilots.

Wireless communication systems often exhibit high delay resolution. However, the existence of fractional Doppler can cause signal distortion, spreading the channel response across multiple Doppler bins. This results in a single target appearing as multiple targets within the DD domain [9]. A Dolph-Chebyshev window design was suggested in [23] to enhance the sparsity of the effective channel in the DD domain, significantly reducing channel spread caused by fractional Doppler effects.

In certain work, such as [24], [25], [26], have investigated channel estimation and data detection in the presence of fractional delay and Doppler shifts. In [24], an iterative Rake decision feedback equalizer for the zero-padded OTFS system was suggested. A unitary approximate message passing detector for OTFS with fractional Doppler was designed in [25]; nevertheless, while employing a rectangular pulse, it adds a cyclic prefix (cp) to each signal. In [26], a sparse Bayesian learning technique was presented for off-grid channel estimation for OTFS, while simultaneously applying the optimal pulse shaping filter. In THz ISAC systems, the channel delay and Doppler parameters need not be restricted to integers to attain high-accuracy sensing.

To address the challenges in the THz ISAC, the waveform design must carefully balance factors such as PAPR, BER, sensing accuracy, Doppler effects, and implementation complexity. In our earlier, shorter version [27], we introduced an EP design scheme and simplified the sensing parameter method from [22] by utilizing the EP design. A dual-stage sensing parameter method was introduced, in which a 2D golden section search efficiently reduced the search space during channel estimation by eliminating the need for iterative feedback. Unlike the iterative approach in [22], our method first estimates the channel parameters then applies them for one-shot data detection. However, despite its effectiveness, this method introduced challenges in sensing accuracy at low SNR. In this paper, we propose a novel super-resolution (SR) OTFS-ISAC framework with EP that overcomes these limitations. Building upon the EP-OTFS concept, the new framework integrates advanced super-resolution techniques into a unified system. Specifically, a super-resolution deep neural network (SR-DNN) is employed to denoise the received signal, thereby enhancing the signal-to-noise ratio (SNR) and enabling more precise path detection. Following denoising, a two-phase channel estimation approach is adopted: the first phase applies the denoising module directly to the DD domain channel matrix, and the second phase uses a max-path step to obtain a coarse estimation of the dominant paths. These initial estimates are then refined through an off-grid search using a low-complexity alternative optimization (AO) technique, referred to as the super-resolution max-path alternative optimization (SR-M-PAO) estimation approach. This integrated process unifies noise reduction, path detection, and channel estimation, significantly enhancing estimation accuracy while reducing computational complexity.

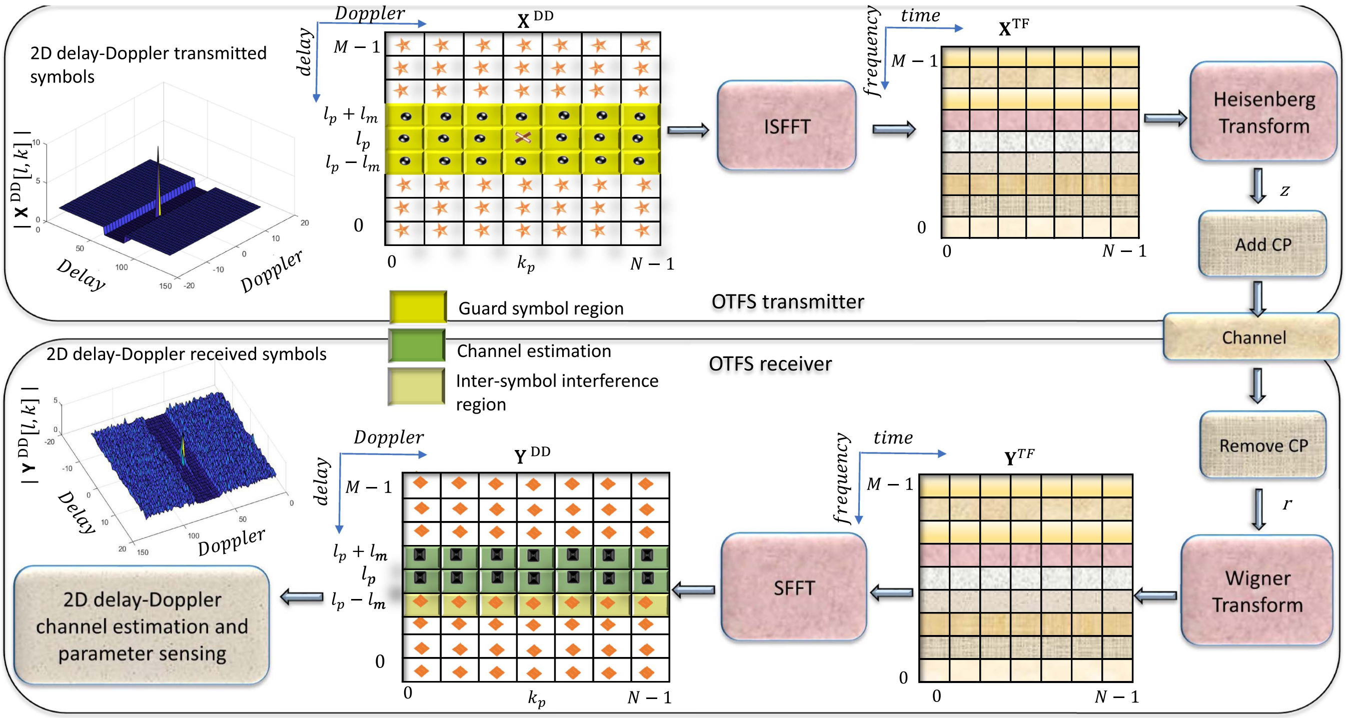

Fig. 1. An illustration of the proposed SR-OTFS-based ISAC framework using a 3-tap channel example. The symbol arrangement is as follows: ✖ represents pilot, ● denotes guard symbols, and ★ indicates data symbols. The received symbol pattern includes ♦ for data detection and ■ for channel estimation.

B. Contributions

The contributions of this work are summarized as follows:

- A novel SR-OTFS framework for ISAC systems has been proposed, specifically designed for multi-target estimation and high-precision transmitter localization. This framework leverages a continuous-delay-and-Doppler-shift (CDDS) channel matrix model, enabling highly accurate DD estimation across both integer and fractional shifts. It inherently integrates an SR-DNN for denoising the received signal and an SR-M-PAO approach for channel estimation, thereby unifying noise reduction, path detection, and channel estimation within a single cohesive system.
- Enhanced PA efficiency and robustness to Doppler effects: Simulations show that the proposed SR-OTFS assisted ISAC framework significantly improves the PA efficiency, achieving about 1.7 dB reduction in PAPR compared to the DFTS-s-OTFS system for 16 quadrature amplitude modulation (16-QAM).
- *High-precision sensing performance:* The proposed SR-OTFS assisted ISAC framework achieves superior sensing performance, providing millimeter-level range estimation accuracy and centimeter-per-second-level velocity estimation accuracy. Simulation results confirm the proposed framework's ability to deliver consistent and reliable performance under both integer and fractional Doppler conditions, resulting in substantial improvements in sensing accuracy relative to the existing OTFS methods.
- *Complexity analysis:* A detailed analysis of the computational complexity of the proposed framework has been performed, specifically calculating the number of real additions and multiplications needed. Simulation results confirm the analytical derivations, showing a substantial reduction in complexity and highlighting the framework's computational efficiency.

This paper is organized into the following sections. Section II describes the SR-OTFS system framework for THz ISAC. The proposed algorithm for estimating sensing parameters and communication channel is detailed in Section III. Section IV presents the simulation results. Lastly, Section V concludes the paper.

Notations: $\mathbb{C}$, $\mathbb{R}$, and $\mathbb{R}_+$ represent the sets of complex numbers, real numbers, and positive real numbers, respectively. The superscripts $(\cdot)^T$ and $(\cdot)^H$ denote the transpose and Hermitian transpose operations, respectively. $\otimes$ denotes the Kronecker product. For an $M \times N$ matrix $\mathbf{X}$, $\mathrm{vec}(\mathbf{X})$, denotes the $MN \times 1$ column vector $\mathbf{x}$ by concatenating the columns of $\mathbf{X}$ in order. The inverse operation, $\mathrm{vec}^{-1}(\mathbf{x})$, reshapes the $MN \times 1$ column vector $\mathbf{x}$ back into an $M \times N$ matrix $\mathbf{X}$. $\mathbf{I}_M$ denotes the $M \times M$ identity matrix. The operator $[\cdot]_q$ denotes the modulo-q operation. $\delta(\cdot)$ is the Dirac delta function. $\lceil \cdot \rceil$ denotes the ceiling function. The operation $\mathrm{diag}\{\cdot\}$ constructs a diagonal matrix from a given vector. The notation $\begin{bmatrix} \cdot \\ \cdot \end{bmatrix}_a$ represents the concatenation of two matrices along the dimension a. The convolution operation is denoted as $*$. $\Re(\cdot)$ and $\Im(\cdot)$ denote the real and imaginary parts, respectively. $||\cdot||_F$ represents the Frobenius norm. Finally, the squared magnitude is denoted by $|\cdot|^2$.

II. System Framework

As shown in Fig. 1, an SR-OTFS-assisted ISAC system with EP is proposed. The transmitter generates a waveform designed to simultaneously support both communication and sensing functions. In passive sensing scenarios, the transmitted signal travels through a combination of line-of-sight (LoS) and multiple non-line-of-sight (NLoS) paths reflected by the sensing targets. Concurrently, the system facilitates information transmission to a communication receiver, which integrates passive sensing and data detection capabilities. The EP within the transmitted signal is leveraged to enhance the accuracy of both sensing and data detection processes.

A. OTFS Transmitter Model Design

Initially, a large number of data frames are generated, each consisting of $M \times N$ information symbols from a Q-ary QAM alphabet, as shown in Fig. 1. The spacing of the subcarrier and the duration of the TF data frame symbols are represented by Δf and T, respectively. M and N denote the number of delay and Doppler bins within the DD domain, respectively. Alternatively, in the TF domain, M and N represent the number of subcarriers and symbols, respectively. When $T\Delta f = 1$, the OTFS signal is critically sampled for any pulse-shaped waveform. The transmitted signal frame has a period of $T_f = NT$ and a bandwidth of $B = M\Delta f$. The DD plane is discretized into a grid of dimensions $M \times N$, denoted as $\mathbf{\Gamma} = \{(\frac{l}{M\Delta f}, \frac{k}{NT}), \quad l = 0, \ldots, M-1, \quad k = 0, \ldots, N-1\}$, where $\frac{1}{M\Delta f}$ and $\frac{1}{NT}$ define the quantization resolutions for the delay and Doppler domains, respectively. Within this grid $\mathbf{\Gamma}$, a pilot symbol and a total of N_g guard symbols are assigned, with $N_g = (2l_m + 1)N - 1$, where l_m represents the maximum normalized delay. The data symbols $\bar{\mathbf{X}}_d[l, k]$ located at location $[l, k]$ are then transmitted within each OTFS frame, as described in [20]. The corresponding overhead due to pilot and guard symbols can be expressed as $((2l_m + 1)N - 1)/MN$. For instance, considering an OTFS frame with parameters $M = 256$ and $N = 64$, and $l_m = 11$, the resulting overhead is approximately 8.97%, which is relatively low and acceptable considering the benefits in sensing performance and estimation accuracy. This demonstrates that the proposed design maintains a favorable trade-off between performance and spectral efficiency.

This arrangement allows the receiver to categorize the received symbols into two distinct groups. The first group, which contains the pilot and guard symbols, is dedicated to channel estimation, while the second group is used for data detection. The region from $l_p - l_m$ to l_p captures the received data symbols that result from the delay spread (worst case l_m) of the transmitted data symbols. The inclusion of guard symbols ensures that the symbols used for data detection remain interference-free from those involved in channel estimation. Consequently, this separation contributes to a more accurate channel estimate, enhancing the quality of data detection within the same OTFS frame. The OTFS frame, represented by $\mathbf{X}^{\mathrm{DD}} \in \mathbb{C}^{M\times N}$ in the DD domain, is composed of two components $\mathbf{X}^{\mathrm{DD}} = \mathbf{X}_d + \mathbf{X}_p$, where $\mathbf{X}_p \in \mathbb{C}^{M\times N}$ is the pilot frame, and $\mathbf{X}_d \in \mathbb{C}^{M\times N}$ corresponds to the data frame, both structured as follows:

$$\mathbf{X}_p[l, k] = \begin{cases} P & l = l_p, k = k_p, \\ 0 & otherwise, \end{cases} \tag{1}$$

$$\mathbf{X}_d[l, k] = \begin{cases} 0 & l_p - l_m \leq l \leq l_p + l_m, \\ & 0 \leq k \leq N-1, \\ \bar{\mathbf{X}}_d[l, k] & otherwise, \end{cases} \tag{2}$$

where l_p and k_p denote the pilot symbol's position on the DD grid and $P = \sqrt{MN\sigma_p^2}$. The average pilot symbol power is given by $E\{|\mathbf{X}_p[l, k]|^2\} = \sigma_p^2$.

The information signal $\mathbf{X}^{\mathrm{TF}} \in \mathbb{C}^{M\times N}$ is then represented in the TF domain by mapping the data symbols using the inverse symplectic finite Fourier transform (ISFFT) [10] as

$$\mathbf{X}^{\mathrm{TF}}[m, n] = \frac{1}{\sqrt{MN}} \sum_{k=0}^{N-1} \sum_{l=0}^{M-1} \mathbf{X}^{\mathrm{DD}}[l, k] e^{j2\pi(\frac{nk}{N} - \frac{ml}{M})}. \tag{3}$$

Then, a Heisenberg transform is applied to the $\mathbf{X}^{\mathrm{TF}}$ signal in order to get $\boldsymbol{z}(t)$ in the time domain as

$$\boldsymbol{z}(t) = \frac{1}{\sqrt{M}} \sum_{n=0}^{N-1} \sum_{m=0}^{M-1} \mathbf{X}^{\mathrm{TF}}[m, n] \mathbf{g}_{tx}(t - nT) e^{j2\pi m\Delta f(t-nT)}. \tag{4}$$

To simulate time-domain (TD) windowing, ideal rectangular pulse-shaping waveforms, $\mathbf{g}_{rx}(t)$ and $\mathbf{g}_{tx}(t)$, are employed. That is, they meet the criterion of the bi-orthogonal property [28], i.e., the cross-ambiguity function $\mathbf{A}_{\mathbf{g}_{rx},\mathbf{g}_{tx}}(t, f) = 0$ for $t \in (nT - \alpha_m, nT + \alpha_m), f \in (m\Delta f - \beta_m, m\Delta f + \beta_m), \forall n, m$, except for $n = 0, m = 0$, where $\mathbf{A}_{\mathbf{g}_{rx},\mathbf{g}_{tx}}(t, f) = 1$ with $t \in (-l_m, l_m), f \in (-\beta_m, \beta_m)$ and α_m, β_m are the maximum actual delay and maximum actual Doppler, respectively.

A single cp is appended to the TD signal of each data frame, expressed by

$$\boldsymbol{z}_{\mathrm{CP}}(t) = \begin{cases} \boldsymbol{z}(t + T_f) & -T_{\mathrm{CP}} \leq t < 0, \\ \boldsymbol{z}(t) & 0 \leq t \leq T_f, \end{cases} \tag{5}$$

where T_{CP} is the duration of the cp.

B. Channel Model

The complex baseband channel impulse response, $\mathcal{H}_w(\alpha, \beta)$, characterizes the TD signal $\boldsymbol{z}(t)$ transmitted over a time-varying channel. For OTFS in the DD domain, the channel's impulse response can be represented as [29]

$$\mathcal{H}_w(\alpha, \beta) = \sum_{i=1}^{L} h_i \delta(\alpha - \alpha_i) \delta(\beta - \beta_i), \tag{6}$$

where L represents the number of paths, and h_i, α_i, and β_i indicate complex path gain, actual delay, and actual Doppler shift associated with the i-th path, respectively. The ranges for delay and Doppler shifts are $\alpha_i \in [0, \frac{1}{\Delta f}]$, $\beta_i \in [-\frac{1}{2T}, \frac{1}{2T}]$, respectively. In the delay-Doppler domain any two paths are resolvable, i.e., $|\alpha_i - \alpha_j| \geq \frac{1}{M\Delta f}$ or $|\beta_i - \beta_j| \geq \frac{1}{NT}$. The corresponding target distance d_i and velocity v_i associated with the i-th path are given by

$$\alpha_i = \frac{d_i}{c_0}, \quad \beta_i = \frac{v_i}{c_0} f_c, \tag{7}$$

where c_0 represents the speed of light and f_c denotes the carrier frequency. The delay and Doppler shift of each path are treated as continuous variables. To capture this characteristic, a continuous-delay-and-Doppler-shift (CDDS) channel matrix is employed, as described in [22].

The continuous signal $\boldsymbol{r}(t)$ is defined as

$$\begin{aligned}\boldsymbol{r}(t) &= \sum_{i=1}^{L} h_i e^{j2\pi\beta_i t}\boldsymbol{z}_{\text{CP}}(t-\alpha_i) + \boldsymbol{w}(t)\\ &= \sum_{i=1}^{L} h_i e^{j2\pi\beta_i t}\boldsymbol{z}([t-\alpha_i]_{NT}) + \boldsymbol{w}(t),\end{aligned} \tag{8}$$

where $\boldsymbol{w}(t)$ represents the additive white Gaussian noise (AWGN), assumed to be independently and identically distributed with zero mean and variance σ_w^2.

The formula for the sampled signal $\mathbf{Z}_{\alpha_i}[l,k]$ of $\boldsymbol{z}([t-\alpha_i]_{NT})$ at $t = kT + \frac{l}{M}T$, where $l = 0,1,\ldots,M-1$ and $k = 0,1,\ldots,N-1$, can be described as

$$\begin{aligned}&\mathbf{Z}_{\alpha_i}[l,k]\\ &= \begin{cases}\frac{1}{\sqrt{M}}\sum_{m=0}^{M-1}\mathbf{X}^{\text{TF}}[m,k]e^{j2\pi m(\frac{l}{M}-\frac{\alpha_i}{T})} & l \geq l_i,\\ \frac{1}{\sqrt{M}}\sum_{m=0}^{M-1}\mathbf{X}^{\text{TF}}[m,[k-1]_N]e^{j2\pi m(\frac{l}{M}-\frac{\alpha_i}{T})} & l < l_i,\end{cases}\end{aligned} \tag{9}$$

where $l_i = \lceil \alpha_i M\Delta f\rceil$. The vector form of $\mathbf{Z}_{\alpha_i}$ is given by

$$\mathbf{z}_{\alpha_i} = \mathbf{\Pi}_{MN}^{l_i}\text{vec}(\mathbf{\Pi}_M^{-l_i}\mathbf{F}_M^H\mathbf{b}_{\alpha_i}\mathbf{X}^{\text{TF}}), \tag{10}$$

where $\mathbf{\Pi}_{MN} \in \mathbb{C}^{MN\times MN}$ is the permutation or forward cyclic-shift matrix, $\mathbf{F}_M^H \in \mathbb{C}^{M\times M}$ is the inverse Fourier transformation matrix of M points, and $\mathbf{b}_{\alpha_i} = \text{diag}\{e^{-j2\pi 0\frac{\alpha_i}{T}},\ldots,e^{-j2\pi(M-1)\frac{\alpha_i}{T}}\}$. By applying the eigen-decomposition property, the cyclic shift matrix $\mathbf{\Pi}_M^{-l_i} \in \mathbb{C}^{M\times M}$ can be decomposed as $\mathbf{\Pi}_M^{-l_i} = \mathbf{F}_M^H\Lambda\mathbf{F}_M$, where $\Lambda = \text{diag}\{e^{j2\pi 0\frac{l_i}{M}},\ldots,e^{j2\pi(M-1)\frac{l_i}{M}}\}$. Thus, (10) can be rewritten as

$$\mathbf{z}_{\alpha_i} = \mathbf{\Pi}_{MN}^{l_i}(\mathbf{I}_N \otimes (\mathbf{F}_M^H\mathbf{B}_{\alpha_i}\mathbf{F}_M))\mathbf{z}, \tag{11}$$

where $\mathbf{B}_{\alpha_i} = \text{diag}\{b^0,b^1,\ldots,b^{M-1}\} \in \mathbb{C}^{M\times M}$ with $b = e^{j2\pi(\frac{l_i}{M}-\frac{\alpha_i}{T})}$. By sampling the continuous signal $\boldsymbol{r}(t)$ in $t = m\frac{T}{M}$ for $m = 0,1,\ldots,MN-1$, the received vector $\mathbf{r} \in \mathbb{C}^{MN\times 1}$ is obtained as

$$\mathbf{r} = \sum_{i=1}^{L} h_i\mathbf{\Delta}^{(\beta_i)}\mathbf{z}_{\alpha_i} + \mathbf{w}, \tag{12}$$

where $\mathbf{\Delta}^{(\beta_i)} = \text{diag}\{e^{j2\pi\beta_i\frac{T}{M}0}, e^{j2\pi\beta_i\frac{T}{M}1},\ldots,e^{j2\pi\beta_i\frac{T}{M}(MN-1)}\}$ is the diagonal matrix of Doppler shifts. Finally, the input-output relationship for the TD baseband signal in (12) can be reformulated as

$$\begin{aligned}\mathbf{r} &= \sum_{i=1}^{L} h_i\mathbf{\Phi}_i\mathbf{z} + \mathbf{w}\\ &= \mathbf{Q}\mathbf{z} + \mathbf{w},\end{aligned} \tag{13}$$

where $\mathbf{\Phi}_i \triangleq \mathbf{\Delta}^{(\beta_i)}\mathbf{\Pi}_{MN}^{l_i}(\mathbf{I}_N \otimes (\mathbf{F}_M^H\mathbf{B}_{\alpha_i}\mathbf{F}_M)) \in \mathbb{C}^{MN\times MN}$ and the TD channel is $\mathbf{Q} = \sum_{i=1}^{L} h_i\mathbf{\Phi}_i \in \mathbb{C}^{MN\times MN}$.

C. OTFS Receiver Model Design

The OTFS receiver, depicted in Fig. 1, processes the received TD signal $\mathbf{r}$ into a delay-time (DT) domain signal matrix given by

$$\mathbf{Y}^{\text{DT}} = \mathbf{G}_{RX}(\text{vec}^{-1}(\mathbf{r})). \tag{14}$$

At the receiver, an ideal rectangular pulse waveform $\mathbf{G}_{RX} = \mathbf{I}_M$ is utilized to maintain compatibility with the OFDM system.

The Wigner transform is then applied to convert the matrix of the DT domain to the TF domain, which is equivalent to DFT when using a rectangular pulse, expressed as $\mathbf{Y}^{\text{TF}} = \mathbf{F}_M\mathbf{Y}^{\text{DT}}$. Subsequently, the SFFT is used to map the TF domain signal $\mathbf{Y}^{\text{TF}}$ back to the DD domain, as follows:

$$\mathbf{Y}^{\text{DD}} = \mathbf{F}_M^H\mathbf{Y}^{\text{TF}}\mathbf{F}_N, \tag{15}$$

where $\mathbf{F}_N \in \mathbb{C}^{N\times N}$ is the Fourier transformation matrix of N points. The received vector in the DD domain, $\mathbf{y}$, is derived by vectorizing $\mathbf{Y}^{\text{DD}}$, expressed as $\mathbf{y} = \text{vec}(\mathbf{Y}^{\text{DD}})$. This vector $\mathbf{y}$ can be expressed as

$$\begin{aligned}\mathbf{y} &= \mathbf{H}\mathbf{x} + \tilde{\mathbf{w}}\\ &= \mathbf{H}\mathbf{x}_d + \mathbf{H}\mathbf{x}_p + \tilde{\mathbf{w}}\\ &= \mathbf{y}_d + \mathbf{y}_p + \tilde{\mathbf{w}},\end{aligned} \tag{16}$$

where $\tilde{\mathbf{w}} = (\mathbf{F}_N \otimes \mathbf{I}_M)\mathbf{w}$ and $\mathbf{x} = \mathbf{x}_p + \mathbf{x}_d$. The terms $\mathbf{x}_d = \text{vec}(\mathbf{X}_d)$ and $\mathbf{x}_p = \text{vec}(\mathbf{X}_p)$ represent vectorized data and pilot matrices, respectively, while $\mathbf{y}_d = \mathbf{H}\mathbf{x}_d$ and $\mathbf{y}_p = \mathbf{H}\mathbf{x}_p$ denote the corresponding outputs after being processed by the channel matrix $\mathbf{H}$. Using (13) and (16), the relation between the channel in DD domain $\mathbf{H} \in \mathbb{C}^{MN\times MN}$ and the channel in TD domain Q can be formulated as

$$\begin{aligned}\mathbf{H} &= (\mathbf{F}_N \otimes \mathbf{I}_M)\mathbf{Q}(\mathbf{F}_N^H \otimes \mathbf{I}_M)\\ &= \sum_{i=1}^{L} h_i\boldsymbol{\rho}_i(\alpha_i,\beta_i),\end{aligned} \tag{17}$$

where $\boldsymbol{\rho}_i(\alpha_i,\beta_i) \triangleq (\mathbf{F}_N \otimes \mathbf{I}_M)\mathbf{\Phi}_i(\mathbf{F}_N^H \otimes \mathbf{I}_M) \in \mathbb{C}^{MN\times MN}$. The structure of the channel matrix $\mathbf{H}$ depends on the channel parameters, i.e., $(\mathbf{h},\boldsymbol{\alpha},\boldsymbol{\beta})$. Specifically, these parameters include $\mathbf{h} = [h_1,h_2,\ldots,h_L]^{\text{T}} \in \mathbb{C}^{L\times 1}$ representing path gains, $\boldsymbol{\alpha} = [\alpha_1,\alpha_2,\ldots,l]^{\text{T}} \in \mathbb{R}_+^{L\times 1}$ denoting path delays, and $\boldsymbol{\beta} = [\beta_1,\beta_2,\ldots,\beta_l]^{\text{T}} \in \mathbb{R}^{L\times 1}$ representing Doppler shifts. After the receiver processing, the system accomplishes passive sensing and data detection with two primary objectives: first, to estimate the channel parameters $(\boldsymbol{h},\boldsymbol{\alpha},\boldsymbol{\beta})$ using $\mathbf{X_p}$ and the received signal $\mathbf{y}$, and then to recover the data matrix $\mathbf{X_d}$, using these estimated parameters.

III. Sensing Parameter Estimation Method

Fig. 2 illustrates a dual-stage method for DD estimation using pilot signals. The first stage applies a denoising module to the EP window in the DD received signal, reducing noise and improving clarity for accurate channel estimation and data detection. The second stage combines a max-path coarse estimation step with an off-grid refinement using a low-complexity AO technique,

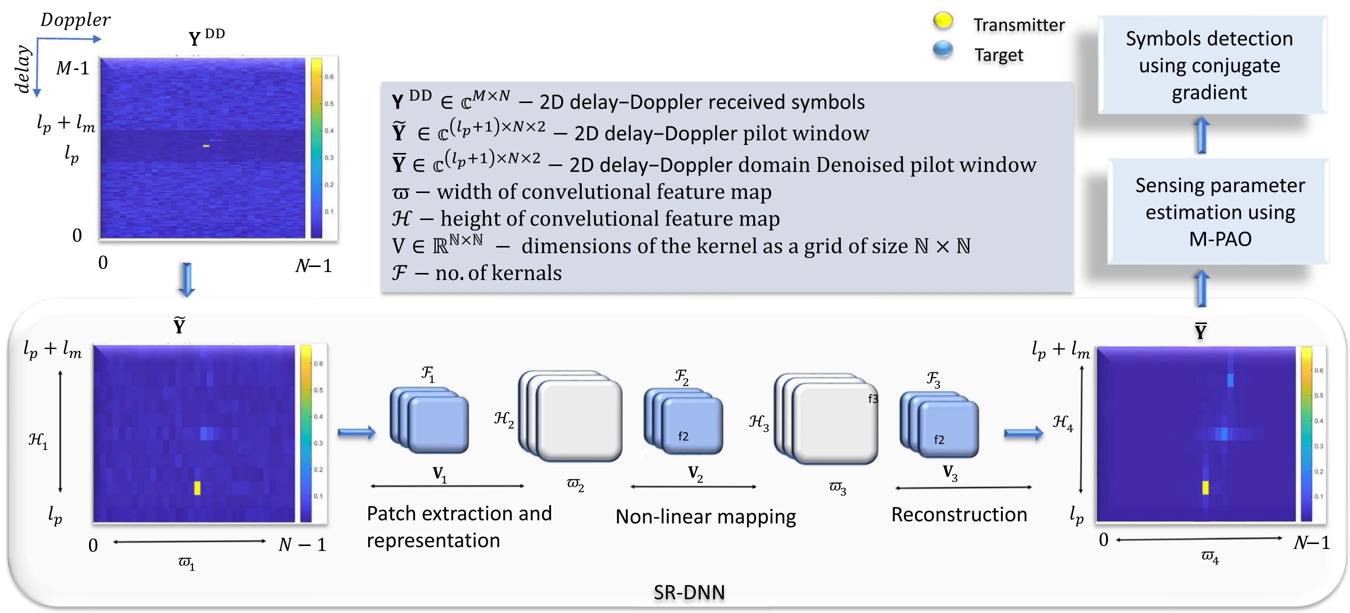

Fig. 2. The proposed denoising module using SR-DNN (example of 2 targets and 1 transmitter state sensing).

known as the M-PAO approach. This method leverages maximum likelihood estimation (MLE) for a high-resolution and precise estimation of DD, even in multipath scenarios.

A. Denoising Using SR-DNN

In OTFS systems, noise degrades channel estimation and data detection, especially in multipath environments with complex DD shifts. Inspired by SR-CNN, which enhances low-resolution images to their high-resolution counterparts [30], the proposed SR-DNN denoises the received signal's pilot window in the DD domain. By suppressing noise while preserving channel path integrity, SR-DNN improves signal quality, enabling more accurate path detection and enhancing OTFS robustness in high-mobility and fractional DD scenarios.

In conventional methods, channel estimation relies on processing the entire received signal matrix $\mathbf{Y}^{\mathrm{DD}}$, which is computationally intensive. To reduce the complexity, the EP structure within the OTFS frame is utilized, allowing efficient separation of pilot and data components. This separation facilitates the development of a low-complexity framework for channel estimation and parameter sensing. By focusing the denoising process solely on the received pilot matrix $\mathbf{Y}_p$ rather than the full received signal matrix $\mathbf{Y}^{\mathrm{DD}}$, the computational demands are significantly reduced without compromising the accuracy of channel estimation.

To estimate the channel state information (CSI) using the received pilot matrix with full guard symbols [20], the received pilot matrix $\mathbf{Y}_p \in \mathbb{C}^{(l_m+1)\times N}$ is defined based on (2) and (16), as follows:

$$\hat{\mathbf{Y}}_p[\tilde{l},k] = \sum_{l'=0}^{l_m} \sum_{k'=-\beta_m}^{\beta_m} \mathcal{T}[l',k']\mathbf{Y}^{\mathrm{DD}}[\tilde{l}-l',k-k'], \quad (18)$$

where $\tilde{l} \in [l_p, l_p+l_m]$ and $\mathcal{T}[l',k'] \in \{0,1\}$ is the path indicator, i.e., $\mathcal{T}[l',k'] = 1$ indicates that there is a path with a delay tap l' and Doppler tap k' with a corresponding path magnitude $\hat{h}[l',k']$. Otherwise, there is no such path, i.e., $\mathcal{T}[l',k'] = 0$ and $\hat{h}[l',k'] = 0$. Then, the total number of paths can be defined as

$$\sum_{l'=0}^{l_m} \sum_{k'=-\beta_m}^{\beta_m} \mathcal{T}[l',k'] = L. \quad (19)$$

Using this structure, the channel estimation process becomes more computationally efficient while maintaining high precision in CSI recovery. The architecture of SR-DNN is shown in Fig. 2, where the input to SR-DNN, $\tilde{\mathbf{Y}} \in \mathbb{R}^{(l_m+1)\times N\times 2}$, is defined as

$$\tilde{\mathbf{Y}} = \begin{bmatrix} \Re(\hat{\mathbf{Y}}_p) \\ \Im(\hat{\mathbf{Y}}_p) \end{bmatrix}_3 . \quad (20)$$

The goal of the network is to denoise $\tilde{\mathbf{Y}}$ and produce an enhanced output $\bar{\mathbf{Y}} \in \mathbb{R}^{(l_m+1)\times N\times 2}$, which provides accurate estimates of the DD shifts. The first layer of the SR-DNN functions as the feature extraction and representation layer. It captures features from the low-resolution input $\tilde{\mathbf{Y}}$ and transforms them into a high-dimensional space. The operation of this convolutional layer can be mathematically described as

$$\mathbf{C}^1 = \sigma(\mathbf{W}_1 * \tilde{\mathbf{Y}} + \mathbf{b}_1). \quad (21)$$

The second layer applies a non-linear transformation to each feature map, generating a high-dimensional representation that corresponds to high-resolution patches

$$\mathbf{C}^2 = \sigma(\mathbf{W}_2 * \mathbf{C}^1 + \mathbf{b}_2). \quad (22)$$

The third layer aggregates the processed patches to reconstruct a high-resolution representation that matches the size of the ground truth channel,

$$\hat{\mathbf{Y}} = \mathbf{W}_{out} * \mathbf{C}^2 + \mathbf{b}_{out}, \quad (23)$$

TABLE I
DENOISING MODULE SETTINGS

Input layer:	real-valued $\tilde{\mathbf{Y}}$ matrix of size $(l_m+1)\times N\times 2$	
Layers	**Operation**	**Filter Size**
1	Conv + ReLU	$64\times(9\times 9\times 2)$
2	Conv + ReLU	$32\times(1\times 1\times 64)$
3	Conv + linear	$2\times(5\times 5\times 32)$
Output layer:	$\tilde{\mathbf{Y}}$ matrix of size $(l_m+1)\times N\times 2$	

where $\mathbf{W}$ is the convolution kernel, $\mathbf{b}$ is the bias term, and $\sigma(.)$ is a non-linear activation function. To train the proposed NN, the Monte Carlo method is employed to generate a dataset consisting of 11×10^4 samples prepared for scenarios involving three targets. The testing phase was conducted in three different scenarios, namely, three targets, two targets, and a single target. The training phase employs the Adam optimizer with a learning rate of 0.001, a batch size of $B=128$, and early stopping is implemented to mitigate overfitting and improve model generalization. Detailed hyperparameters for the SR-DNN layers are outlined in Table I. Building upon the SR-DNN architecture, a denoising module is designed comprising two key phases: an offline training phase, which focuses on optimizing the model parameters using a curated dataset, and an online phase, which ensures that the denoising capabilities are robust and effective.

1) *Offline Training:* The training ground truth matrix $\mathbf{Y}_G\in\mathbb{C}^{(l_m+1)\times N}$ is defined as

$$\mathbf{Y}_G[\tilde{l},k]=\sum_{l'=0}^{l_m}\sum_{k'=-\beta_m}^{\beta_m}\mathcal{T}[l',k']\mathbf{Y}_p[\tilde{l}-l',k-k'],\tag{24}$$

where $\mathbf{Y}_p=\text{vec}^{-1}(\mathbf{y}_p)$. Then, $\mathbf{Y}_G$ can be transformed into a higher-order real matrix as follows:

$$\tilde{\mathbf{Y}}_G=\begin{bmatrix}\Re(\mathbf{Y}_G)\\ \Im(\mathbf{Y}_G)\end{bmatrix}_3,\tag{25}$$

where $\tilde{\mathbf{Y}}_G\in\mathbb{R}^{(l_m+1)\times N\times 2}$. Subsequently, the training dataset is defined as

$$(\tilde{\mathbf{Y}},\tilde{\mathbf{Y}}_G)=\left\{(\tilde{\mathbf{Y}}^1,\tilde{\mathbf{Y}}_G^1),(\tilde{\mathbf{Y}}^2,\tilde{\mathbf{Y}}_G^2),\ldots,(\tilde{\mathbf{Y}}^{N_s},\tilde{\mathbf{Y}}_G^{N_s})\right\}.\tag{26}$$

The training examples are denoted as $\tilde{\mathbf{Y}}^i$ and $\tilde{\mathbf{Y}}_G^i$, where $i\in\{1,2,\ldots,N_s\}$ indicates the i-th instance of the pairs $(\tilde{\mathbf{Y}},\tilde{\mathbf{Y}}_G)$, and N_s denotes the number of training samples. Specifically, the training example $\tilde{\mathbf{Y}}^i$ corresponds to the received pilot signal, while $\tilde{\mathbf{Y}}_G^i$ denotes the associated ground truth values for the i-th frame. Let $f(.)$ represent the function of SR-DNN, with the output given as

$$\mathbf{O}=f(\mathbb{I},\boldsymbol{\Theta}),\tag{27}$$

where $\mathbb{I}$ and $\mathbf{O}$ denote the input and output of SR-DNN, respectively, and $\boldsymbol{\Theta}$ represents the trainable parameters of the SR-DNN. Based on the mean square error (MSE) criterion, the cost function for the offline training phase can be expressed as

$$\Xi(\boldsymbol{\Theta})=\frac{1}{N_s}\sum_{s=1}^{N_s}\|f(\tilde{\mathbf{Y}}^{\mathbf{s}},\boldsymbol{\Theta})-\tilde{\mathbf{Y}}_G^s\|_F^2.\tag{28}$$

The notation $\Xi(.)$ represents the loss function. Consequently, the SR-DNN can refine its trainable parameters through the backpropagation (bp) algorithm, leading to an optimized model characterized by $f(\mathbb{I},\boldsymbol{\Theta}^*)$, where $\boldsymbol{\Theta}^*=\arg\min_{\boldsymbol{\Theta}}(\Xi(f(\mathbb{I},\boldsymbol{\Theta})))$.

2) *Online Prediction:* The received pilot signals $\mathbf{Y}_t\in\mathbb{C}^{(l_m+1)\times N}$ and the testing ground truth values $\mathbf{Y}_{G_t}\in\mathbb{C}^{(l_m+1)\times N}$ can be transformed into higher-order real matrices as follows:

$$\tilde{\mathbf{Y}}_t=\begin{bmatrix}\Re(\mathbf{Y}_t)\\ \Im(\mathbf{Y}_t)\end{bmatrix}_3,\tilde{\mathbf{Y}}_{G_t}=\begin{bmatrix}\Re(\mathbf{Y}_{G_t})\\ \Im(\mathbf{Y}_{G_t})\end{bmatrix}_3,\tag{29}$$

where $\tilde{\mathbf{Y}}_t\in\mathbb{R}^{(l_m+1)\times N\times 2}$ and $\tilde{\mathbf{Y}}_{G_t}\in\mathbb{R}^{(l_m+1)\times N\times 2}$. Subsequently, the testing data set is defined as

$$(\tilde{\mathbf{Y}}_t,\tilde{\mathbf{Y}}_{G_t})=\left\{(\tilde{\mathbf{Y}}_t^1,\tilde{\mathbf{Y}}_{G_t}^1),\tilde{\mathbf{Y}}_t^2,\tilde{\mathbf{Y}}_{G_t}^2),\ldots,(\tilde{\mathbf{Y}}_t^{N_t},\tilde{\mathbf{Y}}_{G_t}^{N_t})\right\},\tag{30}$$

where $\tilde{\mathbf{Y}}_t^{(i)}$ corresponds to the received pilot signals, while $\tilde{\mathbf{Y}}_{G_t}^{(i)}$ denotes the associated ground truth values for the i-th test sample. The input $\tilde{\mathbf{Y}}_t$ is sent to $f(\mathbb{I},\boldsymbol{\Theta}^*)$, and the denoised output can be obtained using the input-output relationship that can be formulated as

$$\bar{\mathbf{Y}}=f(\tilde{\mathbf{Y}}_t;\boldsymbol{\Theta}^*),\tag{31}$$

where $\bar{\mathbf{Y}}\in\mathbb{R}^{(l_m+1)\times N\times 2}$ is the denoised output matrix. The real-valued matrix is then converted into its complex form as follows:

$$\hat{\mathbf{Y}}=\sum_{\tilde{l}=l_p}^{l_p+l_m}\sum_{k=0}^{N-1}\left(\bar{\mathbf{Y}}[\tilde{l},k,1]+j\cdot\bar{\mathbf{Y}}[\tilde{l},k,2]\right)\tag{32}$$

The SR-DNN-based denoising module is summarized in Algorithm 1.

B. M-PAO DD Estimation

The problem of parameter estimation can be effectively addressed using MLE. However, directly solving the MLE for non-linear systems can be computationally prohibitive. As an alternative, the M-PAO approach is employed to simplify the estimation process. The proposed M-PAO method is designed to jointly estimate the parameters of multiple paths in the presence of interference. It is an iterative approach that decomposes the complex optimization problem into simpler sub-problems, where each parameter is alternately optimized while keeping the others fixed. In comparison to existing methods in the literature, this strategy reduces the computational complexity and enhances the accuracy of the estimate by focusing on the most critical components individually compared to the literature.

1) The integer delay and Doppler for each path, along with the corresponding path coefficient, are estimated based on the denoised signal in (31). First, the integer DD pairs $\hat{l}_i,\hat{k}_i$, and the channel path coefficient $\hat{h}_i$ associated with the i-th propagation path are detected by applying a max-path DD estimation approach over the search area, $\xi_i=\{(\hat{l}_i,\hat{k}_i),\quad 0\le\hat{l}_i\le l_m,\quad -\frac{N}{2}\le\hat{k}_i\le\frac{N}{2}-1\}$. This method identifies the paths

Algorithm 1: SR-DNN Denoising Module.

Offline Training:

Input: Training dataset $(\tilde{\mathbf{Y}}, \tilde{\mathbf{Y}}_G)$

Output: Well-trained model $f(\mathbb{I}, \mathbf{\Theta}^*)$

Initialization: Initialize trainable parameters $\mathbf{\Theta}$ using the HeUniform initializer, $E = 1$, $c = 0$, $(\mathbf{Y}_{\text{train}}, \mathbf{Y}_{G_{\text{train}}}) = \{y_i \in \tilde{\mathbf{Y}}, y_{G_i} \in \tilde{\mathbf{Y}}_G \mid 1 \le i \le \lfloor 0.8N_s \rfloor\}$, $(\mathbf{Y}_{\text{val}}, \mathbf{Y}_{G_{\text{val}}}) = \{y_i \in \tilde{\mathbf{Y}}, y_{G_i} \in \tilde{\mathbf{Y}}_G \mid \lfloor 0.8N_s \rfloor + 1 \le i \le 0.9N_s\}$, $\epsilon = \infty$, $\iota = 10$;

repeat

  Update: $\Xi_E(\mathbf{\Theta}) = \frac{1}{0.8N_s}\sum_{E=1}^{0.8N_s} \|(\mathbf{Y}_{\text{train}}, \mathbf{\Theta}) - \mathbf{Y}_{G_{\text{train}}}\|_F^2$ by bp algorithm;

  Update: $\Xi_{v_E}(\mathbf{\Theta}) = \frac{1}{0.1N_s}\sum_{E=1}^{0.1N_s} \|(\mathbf{Y}_{\text{val}}, \mathbf{\Theta}) - \mathbf{Y}_{G_{\text{val}}}\|_F^2$;

  $\mathbf{\Theta}^* = \arg\min_{\mathbf{\Theta}}(\Xi(f(\mathbb{I}, \mathbf{\Theta})))$;

  if $\Xi_{v_E}(\mathbf{\Theta}) < \epsilon$ **then**

    Update: $\epsilon \leftarrow \Xi_{v_E}(\mathbf{\Theta})$;

    $c \leftarrow 0$;

  else

    $c \leftarrow c + 1$;

  end

  if $c >= \iota$ **then**

    break;

  end

  $E \leftarrow E + 1$;

until *Stopping criteria*;

Online Prediction:

Input: Test dataset $(\tilde{\mathbf{Y}}_t, \tilde{\mathbf{Y}}_{G_t}) = \{y_i \in \tilde{\mathbf{Y}}, y_{G_i} \in \tilde{\mathbf{Y}}_G \mid \lfloor 0.9N_s \rfloor + 1 \le i \le N_s\}$

Output: Denoised signal $\hat{\mathbf{Y}}$

Denoise $\tilde{\mathbf{Y}}_t$ using the well-trained model (see (31));

with the maximum amplitude in the denoised signal, enabling the detection of dominant paths for further refinement.

$$(\hat{l}_i, \hat{k}_i) = \underset{(l_i,k_i)\in\xi_i}{\arg\max}(\hat{\mathbf{Y}}), \tag{33}$$

$$\hat{h}_i = \hat{\mathbf{H}}_p[\hat{l}_i, \hat{k}_i], \tag{34}$$

where $\hat{\mathbf{H}}_p = \hat{\mathbf{Y}}/\hat{\mathbf{X}}_p$ and $\hat{\mathbf{X}}_p[\tilde{l}, k] = \sum_{l'=0}^{l_m}\sum_{k'=-\beta_m}^{\beta_m} \mathcal{T}[l', k']\mathbf{X}_p[\tilde{l} - l', k - k']$. Empirically, it has been observed that most estimation errors after the initial coarse search are within one neighboring bin as mentioned in [22]. Consequently, the estimated delay, $\hat{\alpha}_i$, is bounded between $\frac{\hat{l}_i - 1}{M\Delta f}$ and $\frac{\hat{l}_i + 1}{M\Delta f}$, while the estimated Doppler shift, $\hat{\beta}_i$, is constrained between $\frac{\hat{k}_i - 1}{NT}$ and $\frac{\hat{k}_i + 1}{NT}$. As a result, the uncertainty region is defined, effectively reducing the search space for AO,

$$\varsigma_i = \left\{(\alpha_i, \beta_i),\ \frac{\hat{l}_i - 1}{M\Delta f} \le \alpha_i \le \frac{\hat{l}_i + 1}{M\Delta f},\right.$$
$$\left.\frac{\hat{k}_i - 1}{NT} \le \beta_i \le \frac{\hat{k}_i + 1}{NT}\right\}. \tag{35}$$

2) Based on (16), the super-resolution estimation problem can be formulated as an optimization problem that maximizes a function derived from MLE. This method aims to estimate the parameters of the target paths by maximizing the correlation between the predicted and received signals based on (36). For a target i-th, with parameters $(\hat{h}_i, \hat{\alpha}_i, \hat{\beta}_i)$, the estimator can be formulated as

$$(\hat{\alpha}_i, \hat{\beta}_i) = \underset{(\alpha_i,\beta_i)\in\varsigma_i}{\arg\max} \left|(\boldsymbol{\rho}_i\mathbf{x}_p)^H \mathbf{y}_{i_n}\right|^2, \tag{36}$$

$$\mathbf{y}_{i_n} = \begin{cases} \mathbf{y} & i = 1, \\ \mathbf{y} - \sum_{j=1}^{i-1} \hat{h}_j \boldsymbol{\rho}_j \mathbf{x}_p & i > 1. \end{cases} \tag{37}$$

To estimate the parameters of subsequent targets (i.e., the i-th target for $i = 2, 3, \ldots, L$), the interference from targets that have already been estimated needs to be canceled based on (37). Once the parameters of the first target are determined, its interference is subtracted from the received vector, $\mathbf{y}$. The updated received signal, $\mathbf{y}_{i_n}$, is then utilized to estimate the next target's parameters by applying the estimator from (36). The term $\boldsymbol{\rho}_i\mathbf{x}_p$ can be calculated based on (17) as follows:

$$\boldsymbol{\rho}_i\mathbf{x}_p = \text{vec}^{-1}\left(\mathbf{\Delta}^{(\beta_i)}\text{vec}\left(\mathbf{F}_M^H \mathcal{B}_{\alpha_i} \mathbf{X}_p^{\text{TF}}\right)\right)\mathbf{F}_N \tag{38}$$

where $\mathbf{X}_p^{\text{TF}} = \mathbf{F}_M \mathbf{X}_p \mathbf{F}_N^H$. By focusing on the EP window during target parameter estimation, the overall complexity of the estimator can be significantly reduced without compromising the accuracy of channel estimation. This is because the estimation frame is constrained between l_p and $l_p + l_m$ on the delay axis and from 0 to $N - 1$ on the Doppler axis. As a result, the pilot spreading used for channel estimation stays within the maximum channel spread, ensuring the accuracy of the channel estimation is maintained. Therefore, (36) and (38) can be modified as follows:

$$(\hat{\alpha}_i, \hat{\beta}_i) = \underset{(\alpha_i,\beta_i)\in\varsigma_i}{\arg\max} \left|(\hat{\boldsymbol{\rho}}_i\hat{\mathbf{x}}_p)^H \hat{\mathbf{y}}_{i_n}\right|^2, \tag{39}$$

$$\hat{\boldsymbol{\rho}}_i\hat{\mathbf{x}}_p = \text{vec}^{-1}\left(\hat{\mathbf{\Delta}}^{(\beta_i)}\text{vec}\left(\mathbf{F}_{l_m+1}^H \hat{\mathcal{B}}_{\alpha_i} \hat{\mathbf{X}}_p^{\text{TF}}\right)\right)\mathbf{F}_N, \tag{40}$$

where

$$\hat{\mathbf{y}}_{i_n} = \text{vec}\left(\sum_{l'=0}^{l_m}\sum_{k'=-\beta_m}^{\beta_m} \mathcal{T}[l', k']\mathbf{Y}_{i_n}\left[\tilde{l} - l', k - k'\right]\right),$$

$$\mathbf{Y}_{i_n} = \text{vec}^{-1}(\mathbf{y}_{i_n}),$$

$$\hat{\mathcal{B}}_{\alpha_i} = \text{diag}\left\{e^{-j2\pi 0\frac{\alpha_i}{T}}, \ldots, e^{-j2\pi l_m\frac{\alpha_i}{T}}\right\},$$

$$\hat{\mathbf{X}}_p^{\text{TF}} = \mathbf{X}_p^{\text{TF}}\left[l_p : l_p + l_m, 0 : N - 1\right],$$

$$\mathbf{F}_{(l_m+1)}^H \in \mathbb{C}^{(l_m+1)\times(l_m+1)},$$

$$\hat{\mathbf{\Delta}}^{(\beta_i)} = \text{diag}\left\{e^{j2\pi\beta_i\frac{T}{(l_m+1)}0}, e^{j2\pi\beta_i\frac{T}{(l_m+1)}1}, \ldots,\right.$$
$$\left.e^{j2\pi\beta_i\frac{T}{(l_m+1)}((l_m+1)N-1)}\right\}.$$

The complexity of (40) can be further reduced by decomposing the large diagonal matrix $\hat{\mathbf{\Delta}}^{(\beta_i)} \in \mathbb{C}^{(l_m+1)N\times(l_m+1)N}$ into two smaller matrices $\mathbf{C}^{(\beta_i)} \in \mathbb{C}^{N\times N}$ and $\mathbf{A}^{(\beta_i)} \in \mathbb{C}^{(l_m+1)\times(l_m+1)}$, such that $\hat{\mathbf{\Delta}}^{(\beta_i)} = \mathbf{C}^{(\beta_i)} \otimes \mathbf{A}^{(\beta_i)}$. Then, (40) can be represented as

$$\hat{\boldsymbol{\rho}}_i \hat{\mathbf{x}}_p = \text{vec}^{-1}\left((\mathbf{C}^{(\beta_i)} \otimes \mathbf{A}^{(\beta_i)}) \text{vec}(\mathbf{D}^{(\alpha_i)}) \right) \mathbf{F}_N$$
$$= \mathbf{A}^{(\beta_i)} \mathbf{D}^{(\alpha_i)} \mathbf{C}^{(\beta_i)} \mathbf{F}_N, \tag{41}$$

where

$$\mathbf{A}^{(\beta_i)} = \text{diag}\{s^0, s^1, \ldots, s^{l_m}\},$$
$$\mathbf{C}^{(\beta_i)} = \text{diag}\{s^0, s^{(l_m+1)}, s^{2(l_m+1)}, \ldots, s^{(l_m+1)(N-1)}\},$$
$$s = e^{j2\pi\beta_i T/(l_m+1)},$$
$$\mathbf{D}^{(\alpha_i)} = \mathbf{F}_{l_m+1}^H \hat{\mathcal{B}}_{\alpha_i} \hat{\mathbf{X}}_p^{\text{TF}} = \mathbf{F}_{l_m+1}^H \hat{\mathcal{B}}_{\alpha_i} \mathbf{F}_{l_m+1} \hat{\mathbf{X}}_p \mathbf{F}_N^H.$$

The reduced complexity estimator can be expressed in its final form as

$$(\hat{\alpha}_i, \hat{\beta}_i) = \underset{(\alpha_i, \beta_i) \in \varsigma_i}{\arg\max} \left| \left(\mathbf{A}^{(\beta_i)} \mathbf{D}^{(\alpha_i)} \mathbf{C}^{(\beta_i)} \mathbf{F}_N \right)^H \hat{\mathbf{y}}_{i_n} \right|^2. \tag{42}$$

The off-grid search is then performed using the AO algorithm using the objective function (42) over the defined region ς_i.

The steps of the proposed approach are summarized in Algorithm 2. For multi-target estimation, the interference signal from the previously estimated $(i-1)$-th targets is removed while estimating the parameters for the i-th target. The max-path DD estimation method is initially employed to determine the integer parts of the delay and Doppler parameters, as described in (33). Once the integer components are identified, the channel coefficient parameters are calculated based on (34). Subsequently, the fractional DD parameters are refined through applying the AO search method to solve the objective function in (42). The M-PAO approach enhances the precision of multi-target channel estimation by systematically addressing interference and optimizing the estimation process for each target. This ensures robust performance, particularly in scenarios with significant multipath interference and complex DD dynamics.

Algorithm 2: The Proposed M-PAO Algorithm.

Input: Received vector $\hat{\mathbf{y}}_{i_n}$, $\hat{\mathbf{X}}_p$.
Output: Estimated channel parameters $(\hat{\boldsymbol{h}}, \hat{\boldsymbol{\alpha}}, \hat{\boldsymbol{\beta}})$.
Initialization: $\mathbf{y}_{ni} = \hat{\mathbf{y}}_{i_n}$, δ_l, δ_k;
Set $t_d = 1$, $t_p = 1$
for $i = 1 : L$ **do**
  Solve (Eq. 34), (Eq. 33) and obtain $(\hat{h}_i, \hat{l}_i, \hat{k}_i)$;
  $a_1 = \hat{l}_i - 1$, $b_1 = \hat{l}_i + 1$;
  $a_2 = \hat{k}_i - 1$, $b_2 = \hat{k}_i + 1$;
  $L_{\alpha_i} = a_1 : \delta_l : b_1$, $L_{\beta_i} = a_2 : \delta_k : b_2$, select randomly $\alpha_i \in \frac{L_{\alpha_i}}{M\Delta f}$;
  repeat
    Buffer: $\zeta_1 = [\cdot]$, $n = 1$;
    for $j = 1 : \text{length}(L_{\beta_i})$ **do**
      $\beta_j = \frac{L_{\beta_i}(j)}{NT}$
      $\zeta_1(n) = |\mathbf{A}^{(\beta_j)} \mathbf{D}^{(\alpha_i)} \mathbf{C}^{(\beta_j)} \mathbf{F}_N)^H \mathbf{y}_{ni}|^2$;
      $n \leftarrow n + 1$;
    end
    Find: $q_{\max} = \arg\max\{\zeta_1\}$;
    Update: $\beta_i = \frac{L_{\beta_i}(q_{\max})}{NT}$;
    Buffer: $\zeta_2 = [\cdot]$, $n = 1$;
    for $j = 1 : \text{length}(L_{\alpha_i})$ **do**
      $\alpha_j = \frac{L_{\alpha_i}(j)}{M\Delta f}$
      $\zeta_2(n) = |\mathbf{A}^{(\beta_i)} \mathbf{D}^{(\alpha_j)} \mathbf{C}^{(\beta_i)} \mathbf{F}_N)^H \mathbf{y}_{ni}|^2$;
      $n \leftarrow n + 1$;
    end
    Find: $q_{\max} = \arg\max\{\zeta_2\}$;
    Update: $\alpha_i = \frac{L_{\alpha_i}(q_{\max})}{M\Delta f}$;
  until *Stopping criteria*;
  $\hat{\alpha}_i = \alpha_i$, $\hat{\beta}_i = \beta_i$;
  Update $\mathbf{y}_{ni} \leftarrow \mathbf{y}_{ni} - \hat{h}_i \hat{\boldsymbol{\rho}}_i(\hat{\alpha}_i, \hat{\beta}_i) \hat{\mathbf{x}}_p$;
end

C. Complexity Analysis

The computational complexity of the proposed denoising module, utilizing the SR-DNN and the M-PAO estimation algorithm, is evaluated in terms of real additions and multiplications. For the SR-DNN, the computational complexity is determined based on the convolution operations and can be expressed as follows:

$$R_{A_{DM}} = H'W'C_{\text{out}}[(K_h K_w C_{\text{in}}) - 1], \tag{43}$$
$$R_{M_{DM}} = H'W'C_{\text{out}}(K_h K_w C_{\text{in}}), \tag{44}$$

where H' and W' represent the output height and width, C_{out} denotes the number of output channels, K_h and K_w are the kernel height and width, and C_{in} represents the number of input channels.

For the proposed M-PAO algorithm, the computational complexity is reduced as described in (42). The matrix vector operations involved in the objective function for the delay search at a constant Doppler, for each iteration, require $[2\Upsilon \log(l_m + 1) + \Upsilon \log(N) + 2\Upsilon] + n_k[8\Upsilon + \Upsilon \log(n)]$ for real additions and $[\Upsilon \log(l_m + 1) + \frac{\Upsilon}{2} \log(N) + 4\Upsilon] + n_k[12\Upsilon + \frac{\Upsilon}{2} \log(l_m + 1) + 4]$ for real multiplications. Similarly, for the Doppler search with constant delay, the number of real additions and multiplications is $n_l(8\Upsilon + \Upsilon \log(N))]$ and $n_l(12\Upsilon + \frac{\Upsilon}{2} \log(N) + 4)]$, respectively. Therefore, the total number of real additions $R_{A_{M\text{-}PAO}}$ and multiplications $R_{M_{M\text{-}PAO}}$ required for the proposed M-PAO algorithm is respectively given by

$$R_{A_{M\text{-}PAO}} = I\left[(2\Upsilon \log(l_m + 1) + \Upsilon \log(N) + 2\Upsilon) \cdot (n_l + 1) + (n_k + n_l)(8\Upsilon + \Upsilon \log(N))\right], \tag{45}$$

$$R_{M_{M\text{-}PAO}} = I\left[\left(\Upsilon \log(l_m + 1) + \frac{\Upsilon}{2} \log(N) + 4\Upsilon\right) \cdot (n_l + 1) + (n_k + n_l)\left(12\Upsilon + \frac{\Upsilon}{2} \log(N) + 4\right)\right], \tag{46}$$

where I is the number of iterations, and n_l and n_k indicate the number of discretized delay and Doppler pins, respectively along with the signal size $\Upsilon = (l_m + 1) \times N$. In the previous

TABLE II
COMPUTATIONAL COMPLEXITY COMPARISON

Algorithm / Complexity	**Real Multiplications**	**Real Additions**
Proposed SR-OTFS	$I[(\Upsilon\log(l_m+1)+\frac{\Upsilon}{2}\log(N)+4\Upsilon)(n_l+1)$ + $(\mathrm{n}_k+n_l)(12\Upsilon+\frac{\Upsilon}{2}\log(N)+4)]+H'W'C_{\text{out}}(K_hK_wC_{\text{in}})$	$I\,[(2\Upsilon\log(l_m+1)+\Upsilon\log(N)+2\Upsilon)(n_l+1)$ + $(\mathrm{n}_k+n_l)(8\Upsilon+\Upsilon\log(N))$
EP-OTFS [30]	$4I\,[\Upsilon\log(\Upsilon)+16\Upsilon]$	$4I\,[2\Upsilon\log(\Upsilon)+10\Upsilon]$
DFT-s-OTFS [24]	$20I\,(MN\log(MN)+16MN)+5MN\log(MN)$	$20I\,(2MN\log(MN)+10MN)+5MN\log(MN)$

TABLE III
SYSTEM PARAMETERS

Notation	**Definition**	**Value**
M	Number of subcarriers	128
N	Number of symbols for one frame	32
f	Carrier frequency	0.3 THz
Δf	Subcarrier spacing	480 KHz
T	Symbol duration	2.083 μs

sensing method proposed for DFT-s-OTFS for THz ISAC, the computational complexity is calculated based on processing the entire frame of size $M \times N$. However, in the proposed ISAC framework supported by SR-OTFS, only $(l_m+1)\times N$ elements need to be processed, significantly reducing the computational complexity compared to using the full frame size of $M \times N$. Furthermore, additional computational efficiency is achieved through the proposed SR-M-PAO estimation technique, which focuses on a low-complexity off-grid search.

Table II presents a detailed computational complexity comparison, in terms of the number of real multiplications and additions, among the proposed SR-OTFS scheme, our previous work EP-OTFS, and the conventional DFT-s-OTFS. The results clearly demonstrate that the SR-OTFS approach achieves the lowest computational complexity among the three, making it more suitable for practical implementation in complexity-constrained THz ISAC systems.

IV. SIMULATION RESULTS

In this section, the performance of the proposed SR-OTFS system with EP is assessed for the THz ISAC system. The evaluation includes key metrics such as PAPR, BER, and sensing accuracy. Additionally, a comparative analysis is provided with the method in [22]. The simulation parameters, outlined in Table III, are tailored for THz applications and adhere to the 5G numerology standards [31], ensuring compatibility with the next-generation communication systems.

A. PAPR Analysis

The PAPR of the continuous-time baseband signal for the proposed SR-OTFS-ISAC transmit signal is evaluated and compared to other waveforms across different modulation schemes. The performance metric for this evaluation is the complementary cumulative distribution function of the PAPR, which measures the probability that the PAPR exceeds a specified threshold, PAPR_0 i.e., $\Pr(\mathrm{PAPR} > \mathrm{PAPR}_0)$. For consistency, all waveforms utilize a rectangular pulse as a transmit pulse. Fig. 3 highlights the PAPR performance at 16-QAM modulation scheme for different values of σ_p^2. Notably, the PAPR value increases with increasing the average pilot power. Also, the SR-OTFS achieves a PAPR of approximately 1.7 dB lower than that of the DFT-s-OTFS for the 16-QAM modulation scheme. This lower PAPR makes the proposed SR-OTFS a more power-efficient option, which is particularly advantageous in power-sensitive scenarios where minimizing PAPR and conserving energy are critical.

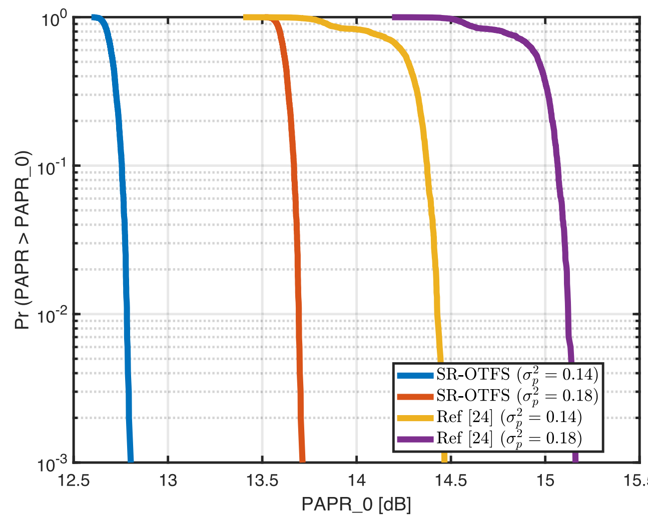

Fig. 3. PAPR comparison for continuous-time baseband signal of the DFT-s-OTFS and SR-OTFS methods.

B. Sensing Performance and BER Evaluation

The sensing accuracy of the SR-OTFS-ISAC is further evaluated using the proposed SR-M-PAO estimation algorithm described in Section III. The performance is assessed using the root MSE (RMSE) as the evaluation metric. The RMSE for the range estimation is defined as $\mathrm{RMSE}(\boldsymbol{\chi}) = \sqrt{\frac{1}{L}\sum_{i=1}^{L}(\chi_i - \hat{\chi}_i)^2}$, where $\boldsymbol{\chi} = [\chi_1, \ldots, \chi_L]$ represents the actual target range values and $\hat{\boldsymbol{\chi}} = [\hat{\chi}_1, \ldots, \hat{\chi}_L]$ represents their corresponding estimates.

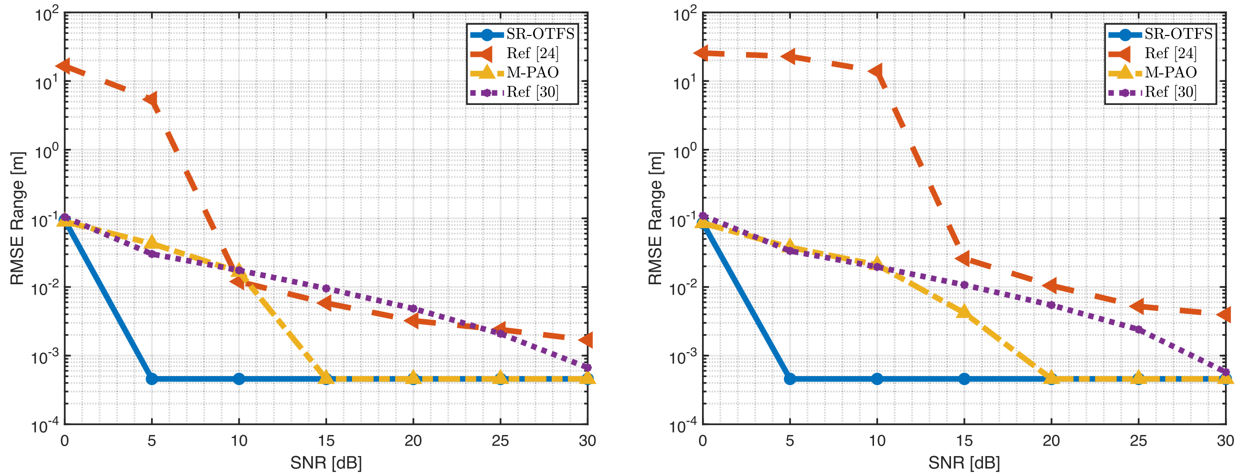

(a) (b)

Fig. 4. Range estimation accuracy comparison using the proposed SR-OTFS, DFT-s-OTFS [22], and EP-OTFS [27] methods. (a) $4-QAM$. (b) $16-QAM$.

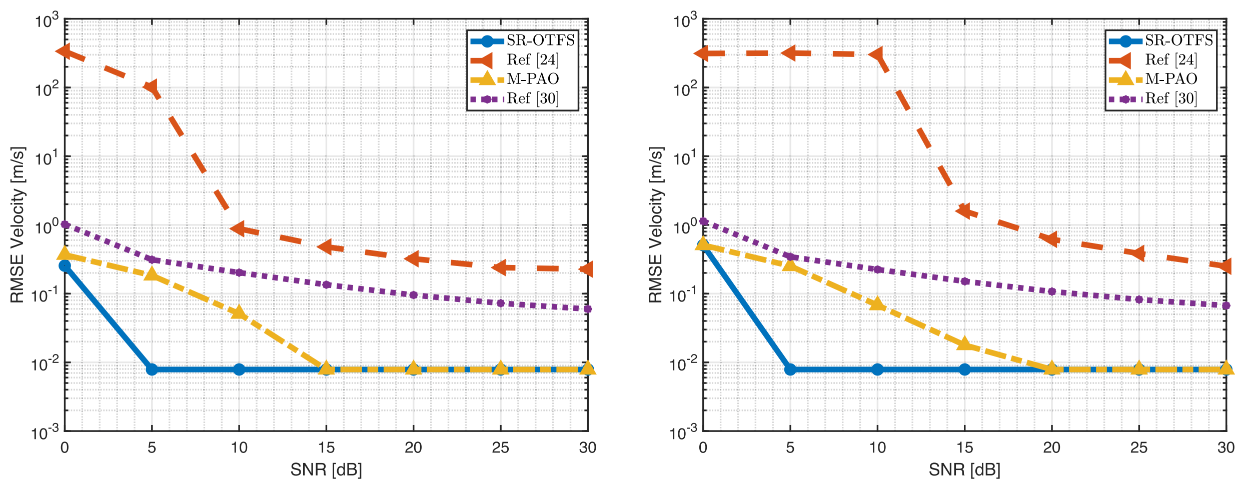

(a) (b)

Fig. 5. Velocity estimation accuracy comparison using the proposed SR-OTFS, DFT-s-OTFS [22], and EP-OTFS [27] methods. (a) $4-QAM$. (b) $16-QAM$.

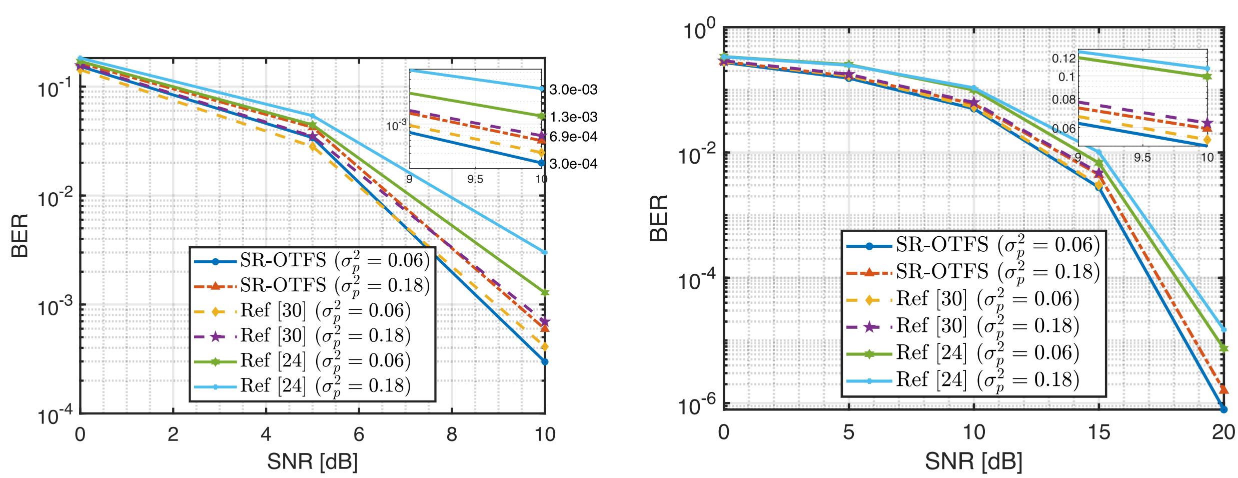

(a) (b)

Fig. 6. BER performance comparison using the proposed SR-OTFS, DFT-s-OTFS [22], and EP-OTFS [27] methods for different values of pilot power. (a) $4-QAM$. (b) $16-QAM$.

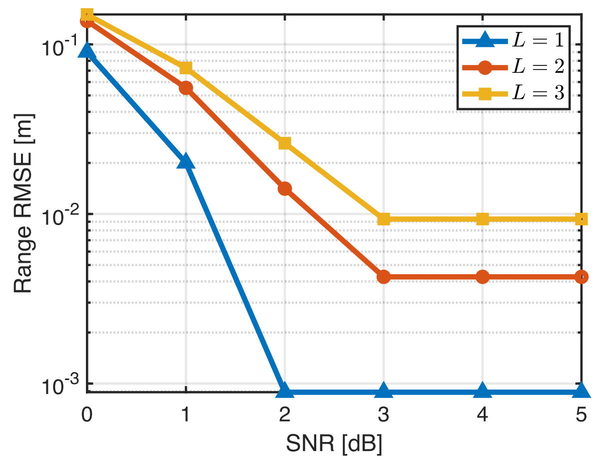

Fig. 7. Range estimation accuracy using the SR-M-PAO estimation method for different numbers of targets.

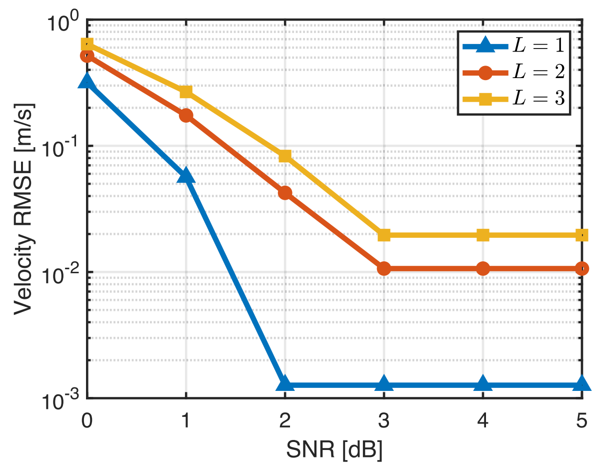

Fig. 8. Velocity estimation accuracy using the SR-M-PAO estimation method for different numbers of targets.

Similarly, the velocity RMSE is defined as $\text{RMSE}(\mathbf{v}) = \sqrt{\frac{1}{L}\sum_{i=1}^{L}(v_i - \hat{v}_i)^2}$, where $\mathbf{v} = [v_1, \ldots, v_L]$ represents the actual target velocity values and $\hat{\mathbf{v}} = [\hat{v}_1, \ldots, \hat{v}_L]$ represents their corresponding estimates.

The analysis considers a doubly selective channel operating at a maximum velocity of 500 km/h [32]. The channel is composed of an LoS path and multiple NLoS paths reflected by the sensing targets. The parameters for the two reference target scenarios are specified as (10 m, 10 m/s) and (40 m, 30 m/s), with 4-QAM, 16-QAM modulation schemes, with $M = 128$ and $N = 32$.

To obtain the distance between the receiver and the target, the channel parameters are first estimated using the proposed SR-M-PAO algorithm. The distance d_s between the sensing target and the receiver in a communication system involving both LoS and NLoS paths can be calculated as [22]

$$d_s = \frac{d_N^2 - d_L^2}{2d_N - 2d_L\cos\theta}, \tag{47}$$

where d_N represents the distance to the NLoS path, d_L indicates the distance to the LoS path, and θ is the angle of intersection between the LoS and NLoS paths. The angle θ plays a crucial role in determining the geometric relationship between these paths. It is important to note that (47) is used to estimate the relative distance between the receiver and the target, not the exact spatial location of the target. This formulation helps compute the root-mean-square error (RMSE), which is used to assess the accuracy of the estimated distances in the simulation results.

Fig. 4 compares the RMSE performance of range estimation across varying SNR levels for the proposed SR-DNN-assisted framework (SR-OTFS), its counterpart without the SR-DNN module (M-PAO), as well as two benchmark schemes: DFT-s-OTFS [22] and EP-OTFS [27]. The evaluation is conducted for both 4-QAM and 16-QAM modulation formats. As seen in both Fig. 4(a) and (b), SR-OTFS achieves a significant reduction in RMSE even at low SNRs (e.g. achieving 10^{-3} m at 5 dB), while other methods only begin to converge at higher SNRs. The advantage is especially pronounced in low-SNR regimes, highlighting the robustness of the SR-DNN module in mitigating noise and enhancing range estimation accuracy.

Furthermore, as illustrated in Fig. 5, The RMSE of velocity estimation is analyzed across various SNR levels for the proposed SR-OTFS framework in comparison with DFT-s-OTFS, M-PAO, and EP-OTFS. The proposed SR-OTFS method consistently outperforms the benchmark methods, which require significantly higher SNRs to approach comparable accuracy. Both Fig. 5(a) and (b), corresponding to the 4-QAM and 16-QAM modulation schemes, respectively, illustrate the superior performance of the proposed SR-OTFS. Notably, the proposed SR-OTFS achieves velocity RMSEs as low as 10^{-2} m/s, demonstrating its robustness and high precision in challenging low-SNR conditions. In contrast, the baseline approaches exhibit much higher RMSE in the low-SNR regime and only gradually converge with increasing SNR, highlighting the effectiveness of the proposed SR-DNN-assisted strategy in enhancing velocity estimation performance.

Fig. 6 compares BER performance of DFT-s-OTFS, EP-OTFS, M-PAO, and SR-OTFS using conjugate gradient equalization for 4-QAM and 16-QAM. The results demonstrate that SR-OTFS outperforms the benchmark methods, primarily due to its more accurate channel estimation and the reduced interference between the channel estimation and data detection regions enabled by the EP design. Additionally, the results show that the BER performance at $\sigma_p^2 = 0.06$ is superior to that at $\sigma_p^2 = 0.18$. This improvement is attributed to the lower pilot power, which reduces leakage into the data region, thereby enhancing data detection and resulting in better BER performance.

Fig. 7 shows the range RMSE of the SR-OTFS-ISAC system using SR-M-PAO with EP for three targets: (10 m, 30 m/s), (30 m, 65 m/s), and (50 m, 90 m/s). With 16-QAM, $M = 128$, and $N = 32$, all targets exhibit low estimation errors at low SNR due to effective denoising. As SNR increases, errors drop significantly, reaching millimeter-level accuracy ($< 10^{-3}$ m) for a single target at SNR > 2 dB. For multiple targets ($L = 2, 3$), RMSE remains below 10^{-2} m despite interference effects.

Fig. 8 shows the velocity RMSE in SR-OTFS-ISAC, achieving millimeter-per-second accuracy for a single target and centimeter-per-second for multiple targets. The results confirm robust, power-efficient operation with early plateauing of

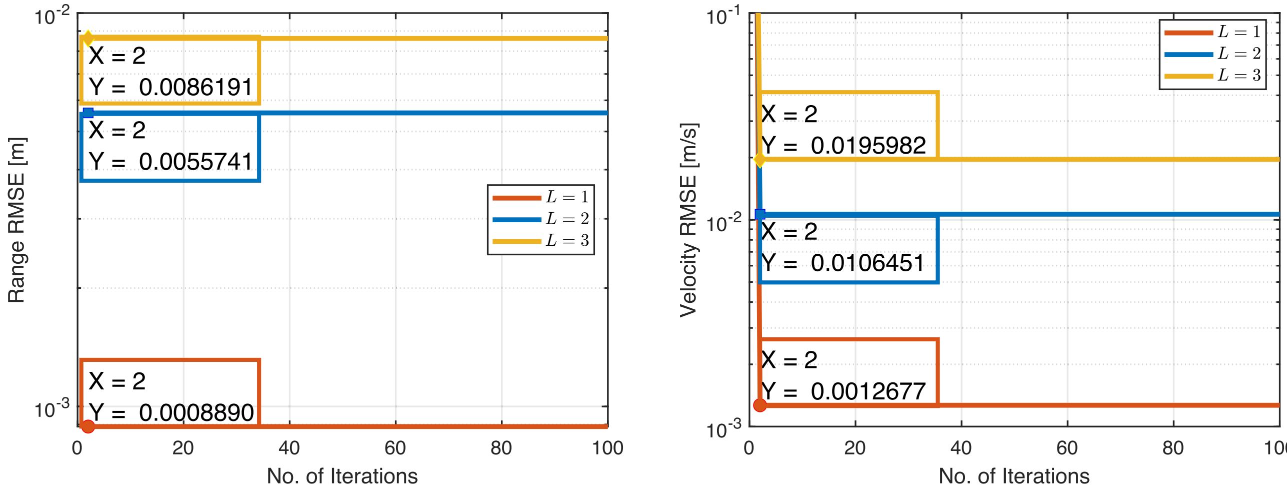

(a) (b)

Fig. 9. Convergence speed of the proposed M-PAO algorithm at SNR = 10 dB. (a) Convergence speed effect on the χ RMSE. (b) Convergence speed effect on the v RMSE.

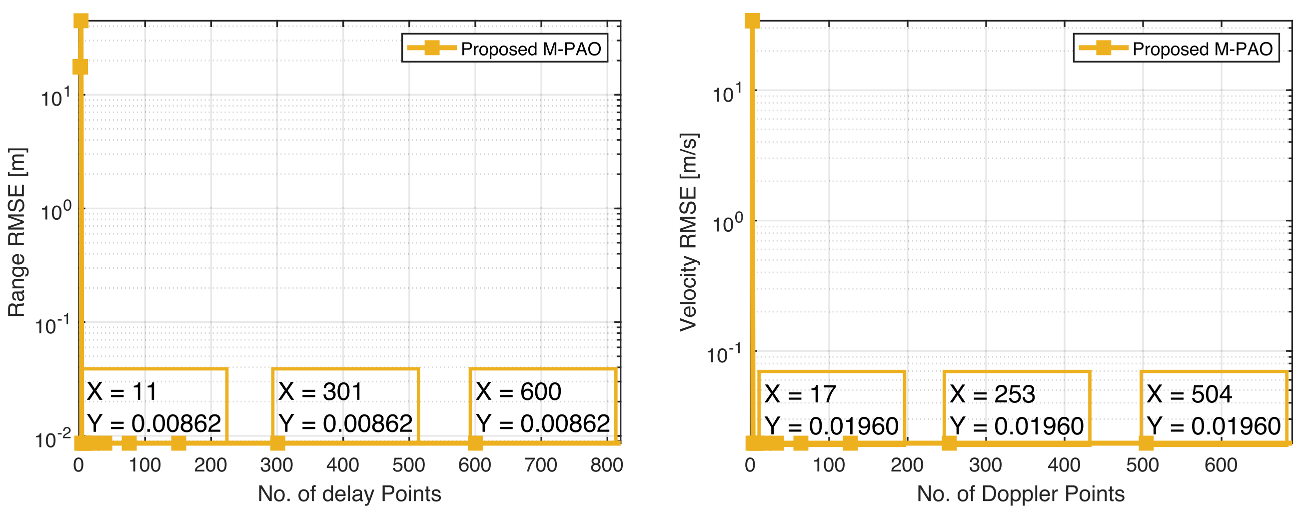

(a) (b)

Fig. 10. Performance of the proposed M-PAO algorithm based on the number of delay and Doppler points at SNR = 10 dB. (a) No. of delay points vs Range RMSE. (b) No. of Doppler points vs Velocity RMSE.

accuracy. The method remains resilient under high modulation orders and mobility, ensuring practical applicability.

C. M-PAO Parameters Analysis

In this section, the parameters of the proposed M-PAO algorithm are analyzed. As shown in Fig. 9, the proposed M-PAO algorithm converges in only two iterations ($I = 2$) to estimate the velocity RMSE of $L = 1$, $L = 2$, and $L = 3$, and in one iteration for the range RMSE. Fig. 9(a) and (b) illustrate the RMSE convergence as the number of iterations increases. For $L = 1$, the algorithm achieves an exceptionally low RMSE of approximately 10^{-3} for both range and velocity. Furthermore, both $L = 2$ and $L = 3$ achieve similarly low RMSE values in just two iterations, demonstrating the rapid convergence of the algorithm. The convergence behavior of the M-PAO algorithm is highly dependent on the choice of hyperparameters. In particular, lower pilot power levels and smaller step sizes generally require a greater number of iterations to achieve convergence. The early convergence observed in some scenarios, such as with pilot power $\sigma_p^2 = 0.14$, $\delta_l = 0.0749$, $\delta_k = 0.0835$, and the initial point set to 10 is not indicative of the algorithm's inherent efficiency, but rather a result of favorable parameter initialization. These hyperparameters provide sufficiently accurate initial estimates, leading to rapid convergence within just two iterations. Therefore, the fast convergence should not be interpreted as a universal outcome of M-PAO, but as a consequence of specific simulation settings that enhance its performance.

The number of delay and Doppler points, n_l and n_k, is determined based on the step size hyperparameters δ_l for delay and δ_k for Doppler in the proposed M-PAO algorithm. In particular, $n_l = \left\lceil \frac{b_1 - a_1}{\delta_l} \right\rceil + 1$ and $n_k = \left\lceil \frac{b_2 - a_2}{\delta_k} \right\rceil + 1$. As shown in Fig. 10, the proposed M-PAO algorithm requires only 11 delay points

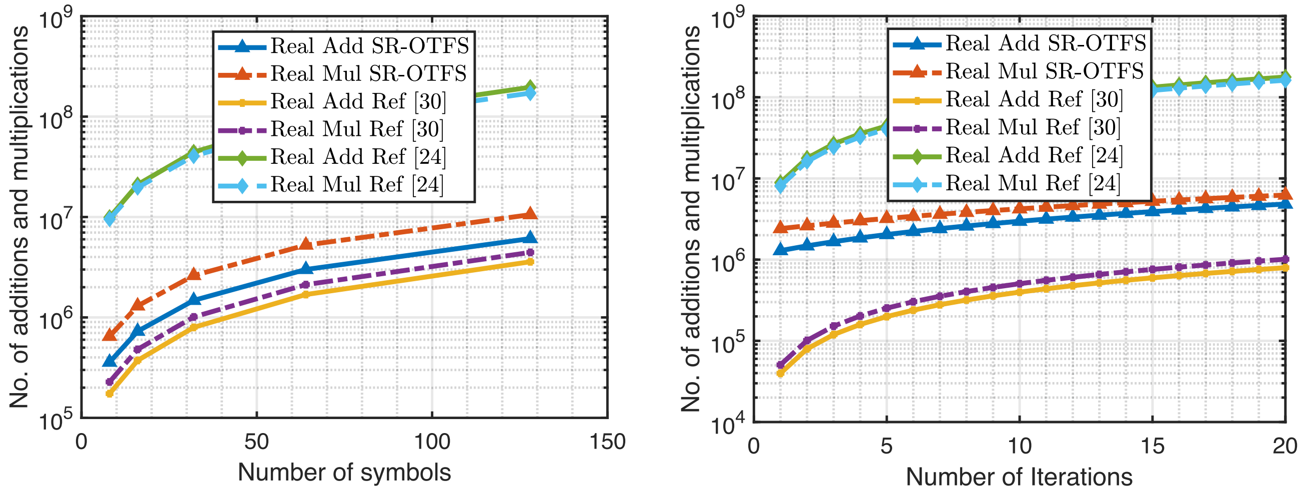

(a)

(b)

Fig. 11. Complexity comparison of the proposed SR-OTFS, DFT-s-OTFS [22], and EP-OTFS [27]. (a) $I = 2$, $n_l = 11$, $n_k = 17$ and $M = 128$. (b) $N = 32$, $n_l = 11$, $n_k = 17$ and $M = 128$.

(i.e., $n_l = 11$) to achieve a range RMSE below 10^{-3} m and 17 Doppler points (i.e., $n_k = 17$) to reach a velocity RMSE of 10^{-2} m/s. This demonstrates the stability and accuracy of the proposed M-PAO algorithm for both range and velocity estimation, requiring only a small number of delay and Doppler points. The rapid convergence, with RMSE values stabilizing early, illustrates the efficiency of the algorithm in minimizing errors across both dimensions with minimal computational effort.

As illustrated in Fig. 11, the proposed SR-M-PAO method significantly reduces computational complexity—measured in terms of real additions and multiplications compared to the DFT-s-OTFS and EP-OTFS schemes. Fig. 11(a) shows that as the number of symbols increases, the complexity gap between SR-M-PAO and DFT-s-OTFS becomes more pronounced, underscoring the superior scalability of SR-M-PAO for systems with large symbol sets. While SR-M-PAO exhibits slightly higher complexity than EP-OTFS due to the additional DNN-based denoising stage, this gap remains relatively small and manageable. Furthermore, Fig. 11(b) demonstrates that the complexity of DFT-s-OTFS rises sharply with the number of iterations, making it impractical for high-iteration scenarios. In contrast, EP-OTFS scales more efficiently, and SR-M-PAO maintains a balanced complexity profile-moderate compared to both benchmarks. As the number of iterations increases, the complexity difference between SR-M-PAO and EP-OTFS narrows, highlighting SR-M-PAO's suitability for systems requiring many iterations, where it offers a favorable trade-off between performance and computational cost.

V. Conclusion

This paper presented a design of an SR-OTFS-ISAC system optimized for THz applications, offering a novel two-stage channel estimation and sensing framework. The proposed framework combined an SR-DNN denoising stage with M-PAO to achieve high accuracy and efficiency in both estimation and sensing. The simulation results showed that the proposed SR-OTFS system effectively reduced the PAPR of the transmitted signal by approximately 1.7 dB compared to the DFT-s-OTFS for 16-QAM modulation. Furthermore, the SR-OTFS system demonstrated high estimation accuracy, achieving millimeter-level range resolution and centimeter-per-second-level velocity resolution, maintaining robust performance even at low SNR levels. The system also outperformed the DFT-S-OTFS benchmark in terms of BER, especially under significant Doppler effects, while achieving a notable reduction in computational complexity due to an efficient estimation algorithm that utilized the EP design. Although a theoretical comparison to the Cramér-Rao Lower Bound (CRLB) was not included due to the complexity of deriving a closed-form expression for the SR-M-PAO scheme with embedded pilots, it remains a valuable direction for future investigation. In general, the proposed SR-OTFS system offered improved estimation accuracy, better BER performance, and reduced complexity, positioning it as a practical and efficient solution for THz ISAC applications.

References

[1] C. Han, Y. Wu, Z. Chen, Y. Chen, and G. Wang, "THz ISAC: A physical-layer perspective of terahertz integrated sensing and communication," *IEEE Commun. Mag.*, vol. 62, no. 2, pp. 102–108, Feb. 2024.

[2] W. Chen, L. Li, Z. Chen, and T. Q. Quek, "Coverage modeling and analysis for outdoor THz networks with blockage and molecular absorption," *IEEE Wireless Commun. Lett.*, vol. 10, no. 5, pp. 1028–1031, May 2021.

[3] S. E. Zegrar, H. Haif, and H. Arslan, "OTFS-based ISAC for super-resolution range-velocity profile," *IEEE Trans. Commun.*, vol. 72, no. 7, pp. 3934–3946, Jul. 2024.

[4] H. Wang et al., "Power amplifiers performance survey 2000-present," 2020. [Online]. Available: https://ideas.ethz.ch/Surveys/pa-survey.html

[5] V. Shatov et al., "Joint radar and communications: Architectures, use cases, aspects of radio access, signal processing, and hardware," *IEEE Access*, vol. 12, pp. 47888–47914, 2024.

[6] U. Demirhan and A. Alkhateeb, "Integrated sensing and communication for 6G: Ten key machine learning roles," *IEEE Commun. Mag.*, vol. 61, no. 5, pp. 113–119, May 2023.

[7] C. Sturm and W. Wiesbeck, "Waveform design and signal processing aspects for fusion of wireless communications and radar sensing," *in Proc. IEEE*, Jul. 2011, vol. 99, no. 7, pp. 1236–1259.

[8] X. Lyu, B. Liu, and W. Fan, "Signal processing in passive radar with multi-user MIMO-OFDM signal," *EURASIP J. Adv. Signal Process.*, vol. 2022, no. 1, Nov. 2022, Art. no. 113.
[9] Z. Wei et al., "Orthogonal time-frequency space modulation: A promising next-generation waveform," *IEEE Wireless Commun.*, vol. 28, no. 4, pp. 136–144, Aug. 2021.
[10] P. Raviteja, K. T. Phan, Y. Hong, and E. Viterbo, "Interference cancellation and iterative detection for orthogonal time frequency space modulation," *IEEE Trans. Wireless Commun.*, vol. 17, no. 10, pp. 6501–6515, Oct. 2018.
[11] L. Gaudio, M. Kobayashi, G. Caire, and G. Colavolpe, "On the effectiveness of OTFS for joint radar parameter estimation and communication," *IEEE Trans. Wireless Commun.*, vol. 19, no. 9, pp. 5951–5965, Sep. 2020.
[12] H. B. Mishra, P. Singh, A. K. Prasad, and R. Budhiraja, "OTFS channel estimation and data detection designs with superimposed pilots," *IEEE Trans. Wireless Commun.*, vol. 21, no. 4, pp. 2258–2274, Apr. 2022.
[13] P. Singh, K. Yadav, H. B. Mishra, and R. Budhiraja, "BER analysis for OTFS zero forcing receiver," *IEEE Trans. Commun.*, vol. 70, no. 4, pp. 2281–2297, Apr. 2022.
[14] F. Liu, Z. Yuan, Q. Guo, Z. Wang, and P. Sun, "Message passing-based structured sparse signal recovery for estimation of OTFS channels with fractional Doppler shifts," *IEEE Trans. Wireless Commun.*, vol. 20, no. 12, pp. 7773–7785, Dec. 2021.
[15] W. Yuan, Z. Wei, J. Yuan, and D. W. K. Ng, "A simple variational Bayes detector for orthogonal time frequency space (OTFS) modulation," *IEEE Trans. Veh. Technol.*, vol. 69, no. 7, pp. 7976–7980, Jul. 2020.
[16] H. Qu, G. Liu, L. Zhang, S. Wen, and M. A. Imran, "Low-complexity symbol detection and interference cancellation for OTFS system," *IEEE Trans. Commun.*, vol. 69, no. 3, pp. 1524–1537, Mar. 2021.
[17] M. K. Ramachandran and A. Chockalingam, "MIMO-OTFS in high-Doppler fading channels: Signal detection and channel estimation," in *Proc. IEEE Glob. Commun. Conf.*, Dec. 2018, pp. 206–212.
[18] R. Hadani and S. Rakib, "OTFS methods of data channel characterization and uses thereof," U.S. Patent 9 444 514 B2, Sep. 2016.
[19] A. Fish, S. Gurevich, R. Hadani, A. M. Sayeed, and O. Schwartz, "Delay-Doppler channel estimation in almost linear complexity," *IEEE Trans. Inf. Theory*, vol. 59, no. 11, pp. 7632–7644, Nov. 2013.
[20] P. Raviteja, K. T. Phan, and Y. Hong, "Embedded pilot-aided channel estimation for OTFS in delay-Doppler channels," *IEEE Trans. Veh. Technol.*, vol. 68, no. 5, pp. 4906–4917, May 2019.
[21] W. Yuan, S. Li, Z. Wei, J. Yuan, and D. W. K. Ng, "Data-aided channel estimation for OTFS systems with a superimposed pilot and data transmission scheme," *IEEE Wireless Commun. Lett.*, vol. 10, no. 9, pp. 1954–1958, Sep. 2021.
[22] Y. Wu, C. Han, and Z. Chen, "DFT-spread orthogonal time frequency space system with superimposed pilots for terahertz integrated sensing and communication," *IEEE Trans. Wireless Commun.*, vol. 22, no. 11, pp. 7361–7376, Nov. 2023.
[23] Z. Wei, W. Yuan, S. Li, J. Yuan, and D. W. K. Ng, "Transmitter and receiver window designs for orthogonal time-frequency space modulation," *IEEE Trans. Commun.*, vol. 69, no. 4, pp. 2207–2223, Apr. 2021.
[24] T. Thaj and E. Viterbo, "Low complexity iterative rake decision feedback equalizer for zero-padded OTFS systems," *IEEE Trans. Veh. Technol.*, vol. 69, no. 12, pp. 15606–15622, Dec. 2020.
[25] Z. Yuan, F. Liu, W. Yuan, Q. Guo, Z. Wang, and J. Yuan, "Iterative detection for orthogonal time frequency space modulation with unitary approximate message passing," *IEEE Trans. Wireless Commun.*, vol. 21, no. 2, pp. 714–725, Feb. 2022.
[26] Z. Wei, W. Yuan, S. Li, J. Yuan, and D. W. K. Ng, "Off-grid channel estimation with sparse Bayesian learning for OTFS systems," *IEEE Trans. Wireless Commun.*, vol. 21, no. 9, pp. 7407–7426, Sep. 2022.
[27] H. I. Hegazy, A. Mohamed, I. Al-Nahhal, and O. A. Dobre, "A low-complexity framework for enhanced sensing and communication in terahertz ISAC systems," *Submitted to IEEE International Conference on Communications (ICC)*, Jan. 2025.
[28] R. Hadani et al., "Orthogonal time frequency space modulation," in *Proc. IEEE Wireless Commun. Netw. Conf.*, Mar. 2017, pp. 1–6.
[29] P. Raviteja, Y. Hong, E. Viterbo, and E. Biglieri, "Practical pulse-shaping waveforms for reduced-cyclic-prefix OTFS," *IEEE Trans. Veh. Technol.*, vol. 68, no. 1, pp. 957–961, Jan. 2019.
[30] C. Vasileiou, J. Smith, S. Thiagarajan, M. Nigh, Y. Makris, and M. Torlak, "Efficient CNN-based super resolution algorithms for mmWave mobile radar imaging," in *Proc. IEEE Int. Conf. Image Process.*, Oct. 2022, pp. 3803–3807.
[31] A. A. Zaidi et al., "Waveform and numerology to support 5G services and requirements," *IEEE Commun. Mag.*, vol. 54, no. 11, pp. 90–98, Nov. 2016.
[32] Y. Wu, C. Han, and Z. Chen, "An energy-efficient DFT-spread orthogonal time frequency space system for terahertz integrated sensing and communication," in *Proc. ICC 2022-IEEE Int. Conf. Commun.*, May 2022, pp. 3484–3489.

Hanem Hegazy (Graduate Student Member, IEEE) received the B.Sc. degree (with Hons.) in electronics and communications engineering, in 2016 from the Faculty of Engineering at Shoubra, Benha University, Cairo, Egypt. She is currently working toward the Ph.D. degree with Memorial University, St. John's, NL, Canada. Her research interests include cybersecurity, wireless communications, smart grid communications, and integrated sensing and communication.

Abdelfatah Abdelbar (Graduate Student Member, IEEE) received the B.Sc. degree (with Hons.) in electronics and communications engineering, in 2016 from the Faculty of Engineering at Shoubra, Benha University, Cairo, Egypt. He is currently working toward the Ph.D. degree with Memorial University, St. John's, NL, Canada. His research interests include wireless communications, visible light communications, and integrated sensing and communication.

Ibrahim Al-Nahhal (Senior Member, IEEE) received the Ph.D. degree in electronics and communications engineering from Memorial University, St. John's, NL, Canada, in 2020. From 2014 to 2015, he was a Physical Layer Expert with Nokia (formerly Alcatel–Lucent), Belgium. From 2021 to 2023, he was a Research Associate and Per-Course Instructor with Memorial University. He is currently an Assistant Professor with the Department of Electrical and Computer Engineering, Memorial University, where he has been a faculty member since 2024. He holds three patents and has coauthored more than 50 peer-reviewed journal and conference papers in top-ranked venues. His research interests include reconfigurable intelligent surfaces, full-duplex communications, integrated sensing and communication, channel estimation, and machine learning for communications. He is the Editor of the IEEE WIRELESS COMMUNICATIONS LETTERS.

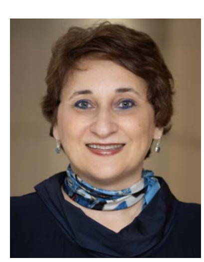

Octavia A. Dobre (Fellow, IEEE) is currently a Professor and Tier-1 Canada Research Chair with Memorial University, St. John's, NL, Canada. She has authored or coauthored more than 600 publications in these areas. Her research interests include wireless communications and networking technologies, as well as optical and underwater communications. She was the recipient of ten Best Paper Awards, including the IEEE Communications Society Heinrich Hertz Award. She is the VP Publications of the IEEE Communications Society. She was the founding Editor-in-Chief of the IEEE OPEN JOURNAL OF THE COMMUNICATIONS SOCIETY and previously was the Editor-in-Chief of IEEE COMMUNICATIONS LETTERS. She is a Clarivate Highly Cited Researcher, a Fellow of the Royal Society of Canada, the Canadian Academy of Engineering, and the Engineering Institute of Canada. She is also an elected member of the European Academy of Sciences and Arts and the Academia Europaea.